

# A Comparison of Climate-Driven Deep Learning Ensemble and SWAT+ Models for Daily Streamflow Simulation in the Niger River Basin, West Africa

Jefia Idolor<sup>1</sup>, Aderemi Adediji<sup>1</sup>, and Peter Adebayo Idowu<sup>1</sup>

<sup>1</sup>Obafemi Awolowo University

April 29, 2024

## Abstract

Streamflow monitoring is very important for planning and management of water resources in watersheds, and their prediction accuracy is crucial for decision-making. The Niger River Basin is a transboundary resource, shared by nine West African Countries and Algeria and, a large portion of the population rely on the basin for rain-fed agriculture and hydropower. Over the years, the basin's streamflow regime has been altered due to climate change, drought, desertification and establishment of Dams. This research describes a novel Deep Learning framework comprised of Bidirectional-Long Short-Term Memory (LSTM) requiring Antecedent Precipitation Index (API) and meteorological variables, preprocessed using Normal Quantile Transform (NQT) as input drivers and, compared with the Soil and Water Assessment Tool (SWAT+) for streamflow prediction. NQT-API-LSTM which considers catchment wetness and seasonality, was forced with reanalyzed climate (1979–2021) while, SWAT+ was driven with biophysical data and reanalyzed climate (2010–2020). The very high performance of both NQT-API-LSTM and SWAT+ models showed the models were reliable and can predict regulated flows with reasonable certainty. However, NQT-API-LSTM outperformed SWAT+ at Lokoja watershed and, realistically captured the influence of seasonal climate and regional groundwater dynamics from upstream catchments including the Sahara Desert on the Benue, Guinean, Sahelian and Sudan Flood. Overall, NQT-API-LSTM could be used successfully for watershed-scale streamflow prediction without the need for continuous ground support data, a benefit for sparsely gauged West African River Basins, while SWAT+ could be used as an alternative, particularly, to evaluate the watershed's response to land use/land cover changes.

## Hosted file

Idolor Adediji Idowu Manuscript.docx available at <https://authorea.com/users/775215/articles/874202-a-comparison-of-climate-driven-deep-learning-ensemble-and-swat-models-for-daily-streamflow-simulation-in-the-niger-river-basin-west-africa>

1 **A Comparison of Climate-Driven Deep Learning Ensemble and SWAT+ Models for**  
2 **Daily Streamflow Simulation in the Niger River Basin, West Africa**

3 **J. J. Idolor<sup>1</sup>, A. Adediji<sup>2</sup>, and P. A. Idowu<sup>3</sup>**

4 <sup>1</sup>Institute of Ecology and Environmental Studies, Obafemi Awolowo University.

5 <sup>2</sup>Department of Geography, Obafemi Awolowo University.

6 <sup>3</sup>Department of Computer Science and Engineering, Obafemi Awolowo University.

7

8 Corresponding author: Jefia Idolor ([jjidolor@gmail.com](mailto:jjidolor@gmail.com))

9 **Key Points:**

- 10 • A climate-driven deep learning ensemble (NQT-API-LSTM) is proposed and compared  
11 to SWAT+ model for watershed-scale streamflow prediction
- 12 • NQT-API-LSTM outperformed SWAT+ and reproduced the streamflow patterns of the  
13 Benue, Guinean, Sahelian and Sudan Flood in Niger River Basin
- 14 • The basin is heavily influenced by seasonal climate and regional groundwater dynamics  
15 from upstream catchments including the Sahara Desert  
16

## 17 **Abstract**

18 Streamflow monitoring is very important for planning and management of water resources in  
19 watersheds, and their prediction accuracy is crucial for decision-making. The Niger River Basin  
20 is a transboundary resource, shared by nine West African Countries and Algeria and, a large  
21 portion of the population rely on the basin for rain-fed agriculture and hydropower. Over the  
22 years, the basin's streamflow regime has been altered due to climate change, drought,  
23 desertification and establishment of Dams. This research describes a novel Deep Learning  
24 framework comprised of Long Short-Term Memory (LSTM) requiring Antecedent Precipitation  
25 Index (API) and meteorological variables, preprocessed using Normal Quantile Transform  
26 (NQT) as input drivers and, compared with the Soil and Water Assessment Tool (SWAT+) for  
27 streamflow prediction. NQT-API-LSTM which considers catchment wetness and seasonality,  
28 was forced with reanalyzed climate (1979–2021) while, SWAT+ was driven with biophysical  
29 data and reanalyzed climate (2010–2020). The very high performance of both NQT-API-LSTM  
30 and SWAT+ models showed the models were reliable and can predict regulated flows with  
31 reasonable certainty. However, NQT-API-LSTM outperformed SWAT+ at Lokoja watershed  
32 and, realistically captured the influence of seasonal climate and regional groundwater dynamics  
33 from upstream catchments including the Sahara Desert on the Benue, Guinean, Sahelian and  
34 Sudan Flood. Overall, NQT-API-LSTM could be used successfully for watershed-scale  
35 streamflow prediction without the need for continuous ground support data, a benefit for sparsely  
36 gauged West African River Basins, while SWAT+ could be used as an alternative, particularly,  
37 to evaluate the watershed's response to land use/land cover changes.

38

## 39 **1 Introduction**

40 Streamflow is a major component of the hydrological processes in the hydrologic cycle,  
41 and it is required for assessment of the distribution, pattern, characteristics and behaviour of river  
42 networks in a watershed. At watershed scale, streamflow serves a crucial role in quantitative and  
43 qualitative monitoring and, control of water resources (Danandeh, 2018). Streamflow data from  
44 watersheds are required for the effective management of water resources (Ni et al., 2020),  
45 irrigation timing and scheduling (Vogel et al., 2015), hydraulic engineering design of  
46 infrastructures such as dams and reservoirs (Amirhossien et al., 2015; Awchi, 2014), river  
47 behaviour analysis (Fryirs & Brierley, 2013) and flood frequency analysis (Jimoh, 2007).  
48 Accuracy in estimation of the timing and volume of streamflow serves as decision-support tools  
49 for policy makers and water resources managers in developing effective water resources  
50 management schemes such as commissioning hydropower dams, timing and allocation of surface  
51 water for irrigation schemes, inland waterways transportation, construction of bridges and  
52 curvets, flood control and drought monitoring.

53 Hydrological models are representations of the physical, chemical and biological  
54 characteristics of the drainage basin catchments and, are used for simulation of basin behavior  
55 and the natural hydrological processes (Duan et al., 2019). Generally, hydrological models  
56 simulate the interactions between the input variables (such as climate data and terrain attributes)  
57 and the system (such as the drainage basin catchments) to estimate an output (such as  
58 streamflow, water level, percolation, soil moisture contents and evapotranspiration).  
59 Hydrological models are employed in estimating low flows which are necessary in watershed  
60 management, and forecasting peak flows which are necessary for flood mitigation (Pfanterstill et

61 al., 2014). The main challenge in the implementation of hydrological models is the diverse  
62 parameters required for calibrating the model, in other to represent all hydrological processes in  
63 a drainage basin more accurately and reduce flood risk errors due to overestimating peak flows  
64 and, prevent water availability problems due to low flows underestimation (Jimeno-Sáez et al.,  
65 2018).

66 In recent times a number of hydrological models have been developed for simulating  
67 river discharges and associated hydrologic components, as well as assessing rainfall-runoff  
68 relationships and, the water balance in drainage basins (Makwana & Tiwari, 2017). Conceptual  
69 hydrological models utilize a number of mathematical formulations in describing the various  
70 processes of the hydrological cycle to simulate streamflow in a watershed (Noori & Kalin, 2016).  
71 The Soil and Water Assessment Tool (SWAT), is a sophisticated numerical model developed by  
72 Arnold et al. (1998) for simulation of the hydrological processes across several climatic and  
73 ecological regions. SWAT is a conceptual semi-distributed model that has gained increasing  
74 popularity within the last two decades for large scale regional hydrological simulation (Grusson  
75 et al., 2017). SWAT model have been employed in several studies to estimate the streamflow  
76 regimes in various watersheds by utilizing diverse spatial and temporal hydrometeorological and  
77 remote sensing data (Jimeno-Sáez et al., 2018).

78 SWAT model can assess and simulate streamflow including nutrients and sediments  
79 transport. SWAT model has been evaluated and validated in drainage basins within the United  
80 States of America and watersheds across the world for hydrologic modeling, pollutant loss, and  
81 climate change research (Arnold et al., 1998). SWAT model's major components are: hydrology;  
82 land use; plant growth; reservoirs; soil; and weather (Arnold et al., 1998). In recent times in the  
83 United States of America, SWAT model is increasingly being adopted for evaluation of the  
84 efficacy of the conservation policy of the United States Department of Agriculture (USDA)  
85 (Mausbach & Dedrick, 2004), for simulation of the Total Maximum Daily Load (TMDL) in  
86 catchments (Borah et al., 2006), for evaluation of hydrological processes at the Upper  
87 Mississippi River Basin, the entire United States of America, and a number of other hydrological  
88 purposes (Arnold et al., 1998). SWAT model has been successfully utilized for modeling the  
89 nitrate-nitrogen loadings and water quality of the raccoon river watershed (Jha et al., 2007).  
90 Adeogun et al. (2018) successfully simulated sediment transport and yield, identified and  
91 prioritized areas susceptible to erosion at the Upper Area of Lake Kainji at the Lower Niger  
92 River Basin in Nigeria and proposed better sediments management plan using SWAT model.  
93 Demirel et al. (2009) reported improvement in daily streamflow simulation accuracy of in data-  
94 scarce regional watersheds using SWAT model.

95 Deep Learning (DL) methods are increasingly becoming accepted as an alternative to the  
96 conventional distributed hydrological models, in simulating complex hydrological processes and  
97 predicting streamflow and water level more accurately. DL is capable of resolving large and  
98 complex tasks such as image classification, nonlinear simulations, time series forecasting, object  
99 detection and pattern analysis by discovering the nonlinear relationships between input data and  
100 the outputs (Hussain et al., 2020). Deep Learning architectures are composed of Artificial Neural  
101 Networks (ANN), and are data-driven approaches with the capability of simulating complex  
102 system dynamics. In recent times, ANNs have been used successfully in research for modeling  
103 complex systems, due to its inherent characteristics such as: being a nonlinear; self-adaptive  
104 data-driven approach; that consist of universal functional approximators; with the capacity to  
105 generalize (Haykin, 1999; Zhang et al., 1998).

106 In the last few years, a number of typical ANN architectures and variants that provide  
107 versatile nonlinear solutions for environmental and water resource challenges have been  
108 developed, such as: Convolutional Neural Networks (CNN); Deep Neural Networks (DNN);  
109 Recurrent Neural Networks (RNN); Gated Recurrent Unit (GRU); Long Short-Term Memory  
110 (LSTM) and; Transformers. These Machine Learning (ML) and DL architectures have been  
111 employed to simulate and forecast streamflow in watersheds. For instance, Hussain, et al. (2020)  
112 utilized extreme learning machine (ELM) and CNN for predicting the daily, weekly and monthly  
113 streamflow for a single step in Gilgit River Basin, Pakistan. According to Hussain, et al. (2020),  
114 the performance metrics indicated that ELM outperformed CNN model with an  $R^2$  score of 0.99  
115 for daily streamflow forecasting between 1980 and 2008. Jimeno-Sáez et al. (2018) applied  
116 ANN and SWAT models to estimate discharge in Miño-Sil and Segura watersheds located in  
117 Peninsular Spain with differing climatic conditions. It was reported that ANNs and SWAT  
118 showed good performance in modeling the daily streamflow of both watersheds. However,  
119 SWAT displayed better skills in predicting low flows, while ANNs showed better skills in  
120 simulating peak flows in the two drainage basins (Jimeno-Sáez et al., 2018).

121 Also, Fu et al. (2020) forecasted streamflow in Kelantan River catchment at the northeast  
122 region of Malaysia Peninsula by utilizing LSTM model. When compared with DNN models,  
123 LSTM models showed better performance in forecast accuracy irrespective of the characteristic  
124 steady dry season flow, or highly variable monsoon flow. According to Fu et al. (2020), the  
125 LSTM model showed expert skills in streamflow estimation in Kelantan River. Van et al. (2020),  
126 used CNN, LSTM and traditional ML models to forecast daily discharge at Can Tho and Chau  
127 Doc sub-catchments of the Vietnamese Mekong Delta. The CNNs and LSTMs models showed  
128 excellent performance in predicting daily rainfall-runoff. However, the CNN model showed  
129 better accuracy for streamflow simulations at both stations. It was reported that there was no  
130 significant contribution from rainfall because the LSTM and CNN models only considered  
131 lagged flows at gauge station. And concluded that CNN and LSTM models had better  
132 performance than conventional methods and, can be adopted as alternatives in other to increase  
133 the accuracy in simulation of hydrological parameters, especially in regulated upstream flows.  
134 ANN and SWAT were employed for forecasting daily streamflow in Pracana Basin and it was  
135 reported that ANN outperformed SWAT model in predicting high flows. SWAT hydrological  
136 model inefficiency in simulating high flows, despite having better mean squared error value, was  
137 attributed to the model formulation (Demirel et al., 2009). Furthermore, ANN, random forest  
138 (RF), Gaussian linear regression model (GLM), Gaussian generalised additive model (GAM),  
139 multivariate adaptive regression splines (MARSs) and 1D-CNN was used by Singh et al. (2023)  
140 for streamflow prediction in Sutlej River Basin and, concluded that RF outperformed other  
141 models in predicting streamflow. Ghorbani et al. (2016) employed support vector machine,  
142 multilayer perceptron (MLP) and radial basis function (RBF) for daily streamflow prediction  
143 whereas, Guo et al. (2011) used support vector machine and ANN for simulation of streamflow  
144 and concluded that support vector machine (SVM) showed better performance in predicting  
145 streamflow. Most recently, Xu et al. (2023) applied transfer learning (TL) Transformer (TL-  
146 Transformer), TL-LSTM, TL-MLP, Transformer, LSTM and MLP for flood modeling in data-  
147 sparse regions in the Yellow River, China.

148 Most physically-based hydrological models are computationally expensive and require  
149 large datasets of hydroclimatic and biophysical attributes for calibration and validation purposes  
150 (Jimeno-Sáez et al., 2018). Even the widely recognized SWAT hydrological model also requires  
151 large datasets comprising of land use, soil, terrain attributes, climate variables and management

152 or decision variables in representing the watersheds hydrological conditions, for estimation of its  
153 CN (curve number) parameter. Hydrological modeling has remained a persistent challenge in the  
154 field of operational hydrology, due to the need to minimize the subjectivity of arbitrarily selected  
155 parameters to represent the physical conditions (Ali et al., 2010). However, these models are  
156 constrained by the limitation of required data for the model's parameter calibration, especially in  
157 sparsely gauged and un-gauged watersheds where data might be missing or inadequate.

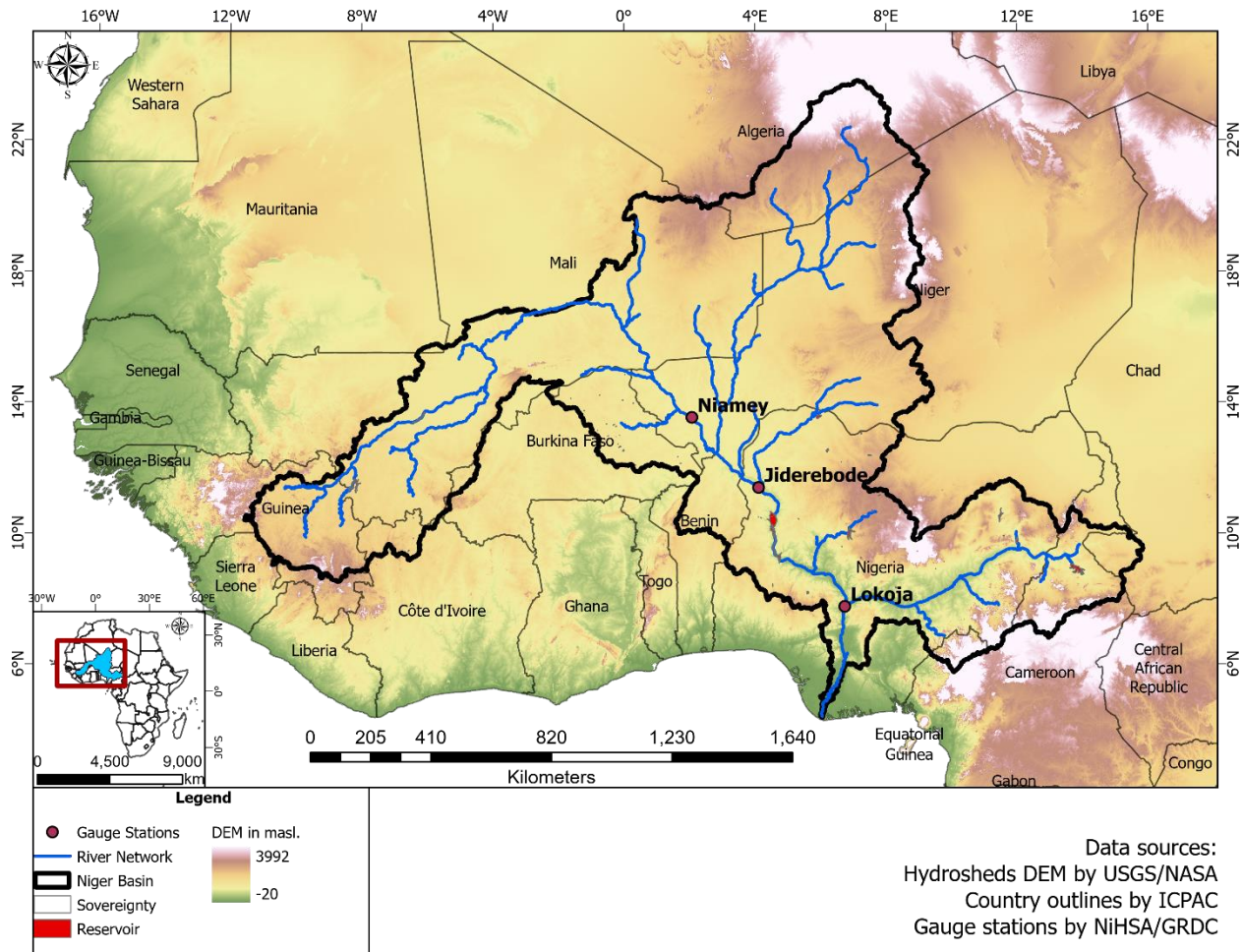
158 The Antecedent Precipitation Index (API), is commonly employed to estimate runoff  
159 from storm events in watersheds where ground-support data is scarce or unavailable. It serves a  
160 crucial role in the estimation of the response of runoff to rainfall, particularly in catchments  
161 where runoff generation is heavily influenced by groundwater and adheres to the principles of  
162 the 'Variable Source Area' concept (Hewlett & Hibbert, 1967). Considerable research attention  
163 has been directed toward API (Descroix et al., 2002) which suggests subjectivity, in determining  
164 the API for representing physical conditions (Ali et al., 2010). Antecedent precipitation refers to  
165 the amount of prior rainfall, affecting the runoff yields of a specific storm event. API represents a  
166 measure of soil moisture index or catchment wetness and frequently remains a parameter  
167 determined subjectively and implemented arbitrarily in modeling runoff response to rainfall  
168 (Heggen, 2001). Recent studies have explored the use of API for simulating runoff yields and  
169 streamflow from storm events (Ali et al., 2010; Descroix et al., 2002; Ghosh et al, 2021). A  
170 number of recent studies have reported improved river discharge and stage forecasting by  
171 including API in the ANN model structure (Dawson & Abrahart, 2007). API, being a numerical  
172 value derived from rainfall depth, can be compared to or used as a proxy for soil moisture. It is a  
173 derived variable that can be incorporated into the modeling framework either as a conventional  
174 'input driver' or as an expert 'output hint'. According to Xia et al. (1997), API can improve the  
175 effectiveness of nonlinear forecasting models, depending on their sophistication.

176 The last few years have seen an increased interest in process-based hydrological models  
177 for streamflow simulation in large West African River Basins (Aich et al., 2015; Poméon et al.,  
178 2018; Schuol et al., 2008). To the best of our knowledge, there are relatively few studies that has  
179 looked specifically at climate-driven deep learning approaches for modeling hydrological  
180 processes at watershed-scale. Thus, in this study, we proposed a novel NQT-API-LSTM  
181 ensemble to be used alongside SWAT+ model for daily streamflow simulation in the Niger River  
182 Basin, a large West African watershed with extremely heterogenous climatic conditions. A  
183 comparison of the performance of NQT-API-LSTM and SWAT+ model was made at the  
184 downstream gauging station at Lokoja. While, the efficiency of NQT-API-LSTM in simulating  
185 the Guinean, Sahelian and Sudan Flood events has been assessed at the Sahelian (Niamey) and  
186 Sudan (Jiderebode) sections of the basin.

## 187 **2 Methodology**

### 188 2.1 The Study Area

189 The study area is the Niger River Basin (NRB) spatially delimited to West Africa within  
190 the boundaries of Benin, Burkina Faso, Cameroon, Chad, Côte d'Ivoire, Guinea, Mali, Niger and  
191 Nigeria and, Algeria (North Africa) as shown in Figure 1. Geographically, it stretches between the  
192 meridians of 11°35'16.99" West and 15°51'44.74" East, from Futa Jallon Highlands in Guinea to  
193 Chad; and between the parallels of Latitudes 4°21'19.60" to 23°54'20.41" North of the equator,  
194 from the Hoggar Mountains in Southern Algeria to the Gulf of Guinea. The headwaters of the



195  
196 Figure 1. Niger River Basin along with Reservoirs, Discharge Stations, DEM and River Network  
197 (6th, 7th and 8th Order Channels)  
198

199 Niger River System originates in the Futa Jallon Highlands in Guinea, and flows north-eastward,  
200 and during the monsoon forms an extensive floodplain in Mali known as the Inland Delta (Inland  
201 *dú Niger*). On leaving the delta, the river meanders in Mali, eventually flowing southeast through  
202 Niger, Benin Republic to Nigeria, and converges with the Benue River at Lokoja and, its waters,  
203 including its sediments and other associated loads such as exotic species are discharged into the  
204 Niger Delta by extensions into the Atlantic Ocean (Lienou *et al.*, 2010). There are 58 large dams  
205 and a total of 260 Dams and Reservoirs with a total volume of  $4.2 \times 10^{10} \text{ m}^3$ , providing various  
206 water resources schemes (irrigation, water supply and hydroelectricity) within the river basin  
207 which have significantly altered the streamflow regime (Lienou *et al.*, 2010). The dams are  
208 irregularly distributed and, mostly concentrated in a few parts of NRB, like Burkina-Faso (where  
209 primarily small-sized dams are found) and Nigeria (where dams of all sizes, including large ones,  
210 exist). The capacity of existing dams ranges from  $25 \times 10^{-3}$  million  $\text{m}^3$  at locations such as Camp  
211 de chasse in Tapoa, Niger to  $1.6 \times 10^{10} \text{ m}^3$  (Kainji, Nigeria). NRB has a total land area of  
212  $2,240,738.61 \text{ km}^2$  and, its stream channel subsystem consists of eight (8) orders ranked from 1<sup>st</sup>  
213 Order to 8<sup>th</sup> Order with the main channel, the Niger River ranked as the 8<sup>th</sup> Order and its largest  
214 tributary channel, the Benue River ranked as the 7<sup>th</sup> Order of NRB. The Niger River, which  
215 stretches approximately 4,200 km, is Africa's third longest river and, ranks as the second largest

216 river in Africa in terms of discharge volume (Oguntunde *et al.*, 2014; Okpara *et al.*, 2013). NRB  
217 encompasses all major climatic regions of West Africa and, the regions are characterized based on  
218 their ecological zones and differing climatic characteristics. The five climatic regions are the  
219 Saharan, Sahelian, Sudan, Guinean, and Guineo-Congolian regions. The Saharan to mid Sahelian  
220 regions of the basin has the driest climatic regime, with average annual rainfall amounts less than  
221 250 mm per year. While, the Guineo-Congolian region is the wettest with rainfall amounts between  
222 2000 mm and 5000 mm. In terms of aridity, NRB encompasses all dryland climate subtypes  
223 (Hyper-arid, Arid, Semi-arid, Dry Subhumid zones) and non-dryland climate subtype (Humid  
224 zone). These climatic zones range from hyper-arid at the Saharan region in the Northern Niger  
225 Basin to humid at the Guineo-Congolian region in the Southern Niger Basin. The climate within  
226 NRB is influenced by the Intertropical Discontinuity (ITD) which by extension influences the  
227 hydrological processes of the river system (Thompson *et al.*, 2017). NRB rainfall scheme is  
228 strongly seasonal and, determined by the Atlantic Monsoon oscillations from May to November.  
229 The magnitude of the Atlantic monsoon event varies greatly between the northern and southern  
230 NRB, but varies uniformly between the eastern and western parts of NRB (Lienou *et al.*, 2010).  
231 The basin exhibits two distinct seasonal rainfall patterns: a unimodal wet season which occurs in  
232 northern NRB and; bimodal wet seasons in southern NRB with a short dry spell between the wet  
233 seasons. Three stream gauges were selected based on data availability and includes: Niamey  
234 gauging station located within the arid Sahelian region of the Middle NRB; Jiderebode gauging  
235 station located within the semi-arid Sudan region of the Lower NRB and; Lokoja gauging station  
236 located within the humid Guinean region of the Lower NRB.

237 The upstream area and major portions of the Upper Niger Basin is characterized by an  
238 ancient geologic landscape of metaigneous rocks followed by metasedimentary crystalline rocks.  
239 These impermeable rocks limits groundwater occurrence, with small aquifer systems occurring in  
240 areas where these rocks are either fractured or are weathered. At the Upper NRB groundwater do  
241 not contribute to the Niger River due to extremely low groundwater recharge from the headwaters  
242 (Fontes *et al.*, 1991). The landscapes of the western bank of Niger River at the Middle NRB are  
243 characterized by the Liptako-Gourma Massif granitic basement (Descroix *et al.*, 2012), while the  
244 sedimentary basin of Iullemeden lies on the right bank of the Niger River, from the Northern Segou  
245 through Gondo depression of the Eastern Dogon region and the Inland Delta (Andersen *et al.*,  
246 2005). The Iullemeden, is a multi-layered aquifer system consisting of the Continental Terminal  
247 dated Eocene to Pliocene overlain by Quaternary and recent dune-like Holocene ergs or alluvium  
248 deposits with aquifer's groundwater hydrologically connected to the Niger River. The Continental  
249 Terminal, is an unbroken aquifer of about 100 m thickness covering tens of thousands of square  
250 kilometers, composed mainly of silty sandstones, clays and sand, with high-quality water. It is the  
251 most significant aquifer in the basin, and borders the Niger River System at Goundam, Timbuktu,  
252 and Gourma Rharous in Mali, Hoggar in Algeria and, extending through Bourem in Gao region in  
253 Mali to Niamey, and Gaya in Niger. Its northern stretch includes the Azaouâd, Taoudenni,  
254 Azaouâk and Tilemsi sedimentary basins. The Continental Shale Band aquifer lies underneath the  
255 Eocene to Cretaceous layers of the Continental Terminal formations and borders the Niger River  
256 at the Northern axis of Benin and also within the arid regions of Mali and Niger. At the Lower  
257 NRB in Nigeria, the watercourse flows along the Continental Terminal whose eastern axis borders  
258 the basin at Jos Plateau in Nigeria and, continues along the Quaternary alluvial deposits on both  
259 the right and left banks of the river at Jebba, and extending through the Benue valley to Cameroon  
260 and Chad. The river then flows alongside artesian aquifers and Cretaceous deposits that continue  
261 to Onitsha. At Onitsha, Tertiary marine layer, then spans across the Cretaceous layer, which are



262 overlaid by saline Quaternary sediments from the coastal region of the Niger Delta. Outside this  
 263 sedimentary basin, crystalline basement complex rock materials dated Precambrian, a constituent  
 264 of the pan-African shield encloses NRB (Andersen et al., 2005; Persits et al., 1997).

265 The hydrological regime of NRB is heavily influenced by groundwater base flow, which  
 266 is affected by annual rainfall and soil permeability. During the dry season, most of the  
 267 contributions occur within the alluvial plains (Andersen *et al.*, 2005). At Benin, the Iullemeden  
 268 discharges into the main channel and its tributaries, and continues along the watercourse  
 269 downstream. In Nigeria, the Rima and Sokoto rivers, ranked as 6<sup>th</sup> and 7<sup>th</sup> order respectively,  
 270 which are the main rivers which drains the Iullemeden (IAEA, 2017), flows into the Niger River,  
 271 just before Jiderebode gauging station. The Niger River Basin System is characterized by four  
 272 major flood events that occurs at various sections of the basin, based on the climatic type which  
 273 includes: the Benue; Guinean; Sahelian and; the Sudan Flood. The Benue Flood event is  
 274 observed at Lokoja confluence, which is mainly associated with the flood waters from the Benue  
 275 River, the largest tributary of the Niger River, whose source lies within the Adamawa Plateau in  
 276 Cameroun, as well as the regulated upstream flows from major Dams which include Jebba,  
 277 Lagdo, Kainji and Shiroro Dams. The Guinean Flood or “black flood” is the main flood from the  
 278 headwaters of the Niger River in Guinea. The Sudan Flood or “white flood” is the local flood  
 279 waters in Jiderebode sub-catchment, and the Sahelian Flood or “red flood” is the local flood  
 280 waters in Niamey sub-catchment.

## 281 2.2 SWAT+ Model

282 This study simulated streamflow at Lokoja sub-catchment of NRB using the updated  
 283 SWAT+ model version 2.2.0 (Bieger *et al.*, 2017). The Soil and Water Assessment Tool (SWAT)  
 284 is a semi-distributed, hydrological process-based river basin model, and can be calibrated to run  
 285 on multiple temporal resolution (daily, monthly or yearly) depending on the time-scale of the  
 286 observation (Arnold *et al.*, 2012). The major constituents of SWAT+ model are: weather,  
 287 hydrology, sedimentation, crop growth, pesticides, soil temperature and properties, nutrients, and  
 288 agricultural management. SWAT model considers the watershed's heterogeneity by subdividing it  
 289 into sub-basins derived from the land use/cover, drainage (river networks), soil properties and  
 290 terrain attributes (such as reservoirs and slope). These sub-basins are subsequently partitioned into  
 291 hydrologic response units (HRUs), representing distinct land areas characterized by distinctive  
 292 combinations of landscape, soil, land use/cover and slope.

293 SWAT+ estimates the components of the water balance by considering the influence of  
 294 climate forcing. The equation representing the water balance is expressed as:

$$SW_t = SW_o + \sum_{i=1}^t (R_i - Q_i - ET_i - Pe_i - QR_i) \quad (1)$$

295 Where  $SW_o$  and  $SW_t$  represents the initial and final soil water content (mm); the index  $t$   
 296 represents time (days);  $R_i$ ,  $ET_i$ ,  $Q_i$ ,  $Pe_i$  and  $QR_i$  represents precipitation, evapotranspiration,  
 297 surface runoff, percolation and baseflow (all units in mm) (Arnold *et al.*, 1998).

### 298 2.2.1 Input Datasets for SWAT+ Model

299 Hourly ERA5 reanalysis climate data for the period of 1979 to 2020 in  $0.25^\circ \times 0.25^\circ$   
 300 grids of (approximately 25 km resolution), which includes temperature, precipitation, dew-point  
 301 temperature, solar radiation, u-wind and v-wind components, were obtained from the European  
 302 Centre for Medium-Range Weather Forecasts (ECMWF) (Muñoz, 2019) and also retrieved from

303 Microsoft Planetary Computer (MPC) data catalog using STAC (Spatio-Temporal Access  
304 Catalog) API (Application Programming interface). The geospatial datasets used in this study  
305 include: HydroSHEDS 3 arc-second resolution (approximately 90 m) hydrologically conditioned  
306 DEM (Lehner et al., 2008; Lehner, 2022), 2 km resolution Harmonized World Soil Database  
307 (HWSD) soil data obtained from the Food and Agricultural Organization (FAO, 2012), ESA  
308 WorldCover 10 m resolution land use/land cover 2020 v100 dataset, made available by the  
309 European Space Agency (ESA) (Zanaga et al., 2021) and retrieved from MPC data catalog using  
310 the STAC API. Streamflow data was obtained from the Nigerian Hydrological Services Agency  
311 (NiHSA) and the Global Runoff Data Centre (GRDC, 2024). Reservoir data was provided by  
312 HydroSHEDS HydroLAKES database version 1.0 (Lehner et al. 2016).

### 313 2.2.2 SWAT+ Model Data Preprocessing

314 In view of computational cost and memory efficiency, HydroSHEDS Hydrologically  
315 conditioned DEM was resampled from 90 m (3 arc-seconds) resolution to 282 m resolution.  
316 While the 10 m resolution ESA Land Use was resampled to 30 m. ERA5 hourly meteorological  
317 reanalysis data was resampled to daily time series. Relative humidity was derived from air  
318 temperature and dew-point temperature according to Sonntag90 method (Sonntag, 1990) and  
319 Wind intensity was derived from the zonal (v-wind) and meridional (u-wind) wind components  
320 before resampling to daily timeseries. A total of 2795 climate data grid points from the  
321 delineated Niger River Basin were used as station data for climate input in SWAT+ model. Data  
322 preprocessing was carried out on node clusters (virtual machine compute instances) linked  
323 together on the backend by Microsoft Azure Kubernetes Services and the frontend by Dask in  
324 Python programming environment. In addition Microsoft Planetary Computer was also used for  
325 Cloud Native data assimilation, data preprocessing and geospatial data analysis using the STAC  
326 (Spatio-Temporal Access Catalog) API (Application Programming interface).

### 327 2.2.3 SWAT+ Model Setup

328 SWAT+ model parametrization was performed using the QSWAT+ interface in QGIS  
329 software. The DEM was used to derive the stream network and delineate the basin and its sub-  
330 basin boundaries. The Soil map was overlaid on the delineated watershed and sub-watersheds to  
331 provide details about soil properties, including soil texture, hydraulic conductivity, and available  
332 water content. Next, the land use/cover map was overlaid on the sub-basins and three slope  
333 categories were defined ( $0 - 3\%$ ;  $> 3\% - 6\%$  and;  $> 6\%$ ). Dominant HRUs option was used to  
334 derive the Hydrological Response Units (HRU) and reservoirs were added. The properties of the  
335 reservoirs included in the SWAT+ model structure in this study is presented in Table 1. Finally,  
336 NRB was subdivided into 11 sub-watersheds and 182 HRUs. The potential evapotranspiration  
337 was determined using the Penman-Monteith method while, the curve number was calculated  
338 using the Muskingum method. The dominant land use/cover distribution for NRB were: barren  
339 (30.36 %), range grasses (28.10 %); agriculture (18.45 %); range-brush (14.76 %); forest (6.83  
340 %); wetland (0.72 %); urban (0.72 %); wetlands water (0.27 %) and; wetlands forested or  
341 mangrove forest (0.00%). The hyper arid, arid and semi-arid climatic condition in the Upper  
342 Sahel and Saharan regions explains the dominance of barren areas in NRB.

343  
344  
345

346 **Table 1: Properties of the Reservoirs within the Niger River Basin which are included in the**  
 347 **SWAT+ model**

Name	River	Year	Long (°)	Lat (°)	Elevation (m)	Surface area (km <sup>2</sup> )	Storage volume (km <sup>3</sup> )
Kainji	Niger	1968	4.56	10.32	110	1034.85	15.00
Lagdo	Benue	1983	13.85	8.89	208	623.12	7.80
Shiroro	Kaduna	1984	6.90	9.98	335	271.12	7.00
Jebba	Niger	1984	4.68	9.36	89	274.76	3.60
Dadin Kowa	Gongola	1988	11.50	10.53	246	150.56	2.86
Selingue	Sankarani	1982	-8.22	11.46	336	335.77	2.17
Goronye	Rima	1983	5.95	13.54	286	107.48	0.98
Kiri	Gongola	1982	12.01	9.76	170	68.52	0.62
Markala	Niger	1947	-6.23	13.50	282	102.32	0.18

348

#### 349 2.2.4 Sensitivity Analysis, Calibration and Validation

350 The hydrometeorological daily time series were split into three periods: warm-up;  
 351 calibration and; validation. The period spanning from 2007 to 2009 was chosen as the warm-up  
 352 phase and followed immediately by the calibration phase spanning from 2010 to 2007. While,  
 353 the validation phase span from 2018 to 2020. Sobol method was used for the sensitivity analysis  
 354 while, automatic calibration of the model's sensitive parameters was done using the Latin  
 355 hypercube algorithm in SWAT+ Toolbox v1.0.1. Sensitivity analysis involved identifying the  
 356 parameters with the strongest influence on streamflow, by varying the model's parameters, and  
 357 estimating the model's output changes in relation to its variations (Arnold *et al.*, 2012). During  
 358 the sensitivity analysis, 2200 iterations was carried-out to obtain the 1<sup>st</sup> order sensitivity for the  
 359 basin. In conducting calibration, daily streamflow observations at Lokoja gauge station was used  
 360 and, involved adjustment of the model's parameters, in other for the daily simulations to  
 361 correspond closely with observations. Automatic calibration was performed using two iterations  
 362 of 1500 simulations with the sensitive parameters and, readjusting the parameters prior to the  
 363 next simulation. The SWAT+ sensitive parameters for calibration and their final values  
 364 considered in this study is shown in Table 2.

#### 365 2.3 Antecedent Precipitation Index (API)

366 The antecedent precipitation index (API) is a hydrological model that accounts for  
 367 amounts of previous rainfall occurrence prior to new storm events. It is a soil moisture index that  
 368 is used in estimating runoff response to rainfall. API is derived from daily rainfall time series  
 369 using the equation expressed as;

$$API = \sum_{t=-1}^{-i} P_t k^{-t} \quad (2)$$

370

371 where  $P_t$  is the rainfall amount on the  $t$ th day prior to the occurrence of the rainfall event (storm),

372

373 **Table 2. Parameters included in SWAT+ model calibration in Lokoja**

Parameter	Sensitive Parameter	Rank	Range	Fitted Value
bd	Moist bulk density (g/cm <sup>3</sup> )	1	0.9 – 2.5	-6.74 %
awc	Available water capacity (mm H <sub>2</sub> O/mm soil)	2	0.01 – 1	-7.98 %
cn2	SCS runoff curve number	3	35 – 95	4.24 %
alpha	Baseflow alpha factor (1/day)	4	0 – 1	-6.12 %
perco	Percolation Coefficient	5	0 – 1	2.31 %
revap_co	Groundwater “revap” coefficient	6	0.02 – 0.2	12.36 %
epco	Plant uptake compensation factor	7	0 – 1	-6.44 %
esco	Soil evaporation compensation factor	8	0 – 1	2.25 %
chk	Hydraulic conductivity	9	-0.01 – 500	5.43 %
flo_min	Minimum aquifer storage to allow return flow (m)	10	0 – 50	2.58 %

374

375 and  $k$  is a constant (Kohler & Linsley, 1951).

376 API for this study was calculated using the daily rainfall ( $P$ ) data for a period of 43 years  
 377 (1979 – 2021) with a constant ( $k$ ) of 0.98 that was within the limits for  $k$  (0.80 – 0.98)  
 378 recommended by Viessman & Lewis (1996).

379 

#### 2.4 Data and Data Preprocessing Techniques

380 The choice of input variables has a significant influence on streamflow simulation and  
 381 forecasting. According to systems theory, system variables can be categorized into three distinct  
 382 categories: input; output and; state variables. State variables are representations of a measure of  
 383 some intrinsic qualities of the system’s condition and, these variables usually exhibit spatial  
 384 variations and changes over time. In a Drainage Basin Systems, state variables include;  
 385 Discharge (streamflow), Stage (water level) and water quality parameters. Input variables are  
 386 further divided into two groups: control variables and random variables. Control variables are  
 387 often referred to as management or decision variables such as irrigation extraction rates, and  
 388 reservoir or dam storage and release schedule. While random variables exhibit statistical  
 389 randomness such as temperature and precipitation. The Output variables represent the future  
 390 state(s) being predicted such as streamflow. In most machine learning applications for  
 391 streamflow forecasting, state variables frequently serve as both input and output, with input and  
 392 output datasets representing the state(s) lag time and lead time respectively. Existing research has  
 393 focused on a combination of previous state(s), as univariate or multivariate inputs, to predict  
 394 future state(s) as output (Van et al., 2020; Xu et al., 2023), but has failed to explore the  
 395 significant influence of meteorological variables on the simulated flow. Thereby limiting the  
 396 Deep Learning model’s ability to learn the causal relationship, behavior and pattern of the  
 397 meteorological variables and their climatic drivers influencing the hydrological processes in the  
 398 watershed. Thus, in this study, reanalysed meteorological variables such as rainfall and  
 399 temperature and, API model outputs were utilized as input drivers in the LSTM model  
 400 development.

401

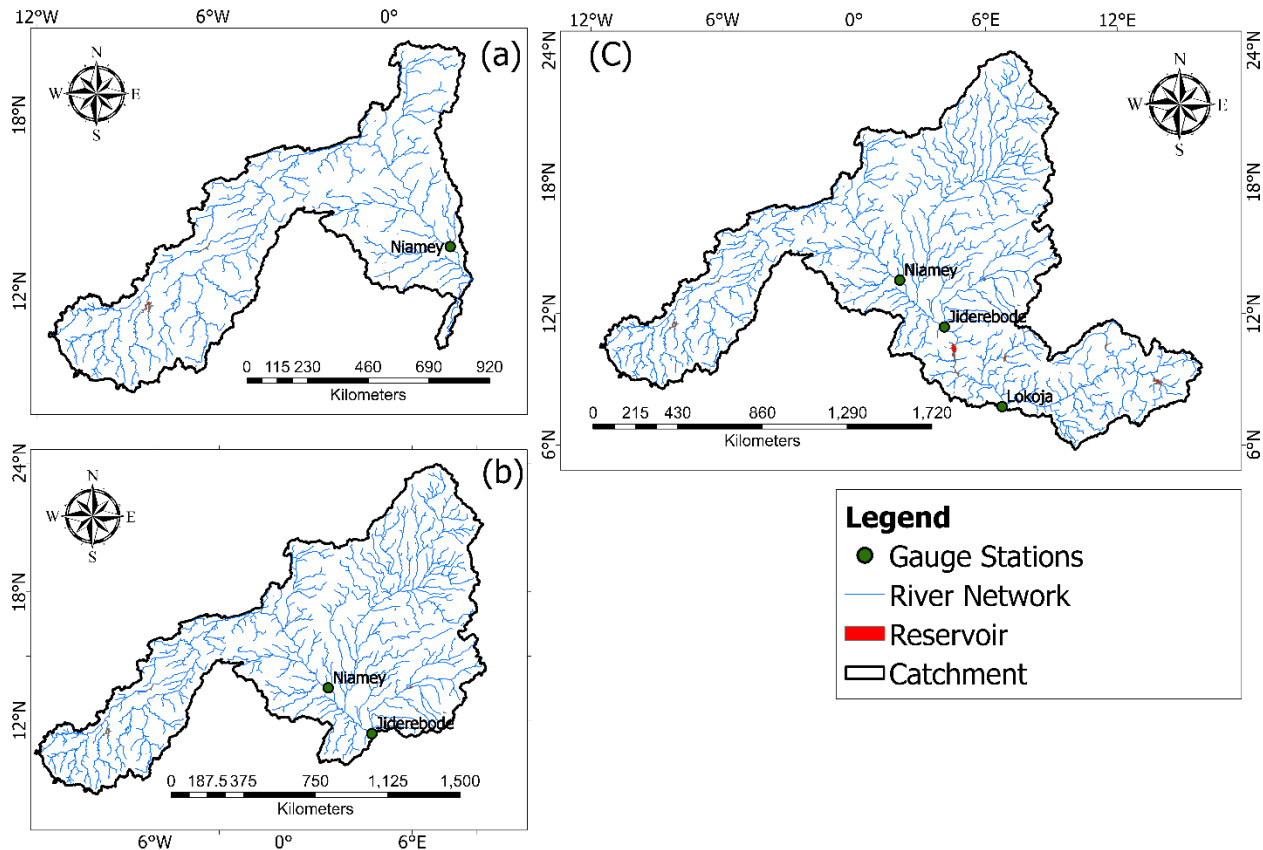


Figure 2. Catchments, reservoirs and drainage network within the Niger River Basin extending to: (a) Niamey gauge station; (b) Jiderebode gauge station and; (c) Lokoja gauge station

#### 2.4.1 Feature Engineering

Hourly ERA5 reanalysis meteorological data spanning from 1979 to 2021 in  $0.25^\circ \times 0.25^\circ$  grids, was resampled to daily time series. The rainfall and temperature data required by the LSTM models was determined using the basin areal average. Since the gridded meteorological data was uniformly distributed, Arithmetic Areal Averaging method, which is based on equal contribution of all grid cells within the watershed was used to determine the basin areal average. In other for the model to accurately describe the spatial characteristics and pattern of the basin's climate, the DEM was delineated into sub-basins using ArcGIS Pro software. And, HyBAS HydroBasins level 4 shapefiles (Lehner and Grill, 2013) were merged within the boundaries of the delineated basins in other to encourage reproducibility. Due to the enormously heterogeneous geomorphology and climatic conditions of the study area (NRB), a single mesoscale modeling framework was developed for each sub-watershed as shown in Figure 2. The Arithmetic Areal Averaging method was applied to the active sub-basins rainfall and temperature data, to generate the input variables (features) for the LSTM models. Features (input variables) for the LSTM models to estimate daily streamflow (target) was generated from the precipitation and temperature time series using time delay embedding such as lag observations and rolling window statistics operation. Firstly, API was calculated for the selected sub-catchments. Other input variables considered in the feature space were: daily mean temperature ( $T_t$ ); daily rainfall ( $P_t$ ); lag rainfall ( $P_{t-n}$ ); lagged temperature ( $T_{t-n}$ ), rolling total rainfall ( $R_n$ ) and; rolling mean

425 temperature ( $T_m$ ). LSTM model development is dependent on the spatial-temporal relationships  
 426 between streamflow and climate dynamics. Similar to previous studies, the time delay  
 427 embedding for the input variables (features) were determined using cross-correlation analysis to  
 428 assess the temporal relationships between rainfall, temperature and streamflow (Amirhossien *et*  
 429 *al.*, 2015; Jimeno-Sáez *et al.*, 2018).

#### 430 2.4.2 Feature Selection

431 Feature space that comprises of large numbers of features (input variables) or highly  
 432 correlated features, may lead to unacceptably high variance and reduction in prediction accuracy.  
 433 Sparsity constraints can be applied on the feature space to prune uninformative covariates which  
 434 do not influence the outputs. The Least Absolute Shrinkage and Selection Operator (LASSO) is a  
 435 regression model introduced by Tibshirani (1996), which allows both continuous shrinkage and  
 436 variable selection by utilizing an  $L1$ -norm sparsity constraint to enforce the coefficients of least  
 437 important covariates to zero and retains only important features. The LASSO formulation is  
 438 shown as follows:

$$\sum_{i=1}^n (y_i - \sum_j x_{ij} \beta_j)^2 + \lambda \sum_{j=1}^p |\beta_j| \quad (3)$$

439 where  $x_{ij}$  are the standardized features (input variables) and  $y_i$  are the response variables (targets)  
 440 for  $i = 1, 2, \dots, N$  and  $j = 1, 2, \dots, p$ ,  $\beta_j$  represent the coefficient of the  $j$ -th feature.  $\lambda \sum_{j=1}^p |\beta_j|$   
 441 is the the  $L1$  penalty, also known as the Lasso penalty, and it is controlled by the hyperparameter  
 442  $\lambda$ , which adjusts the strength of the penalty term. In Lasso regression, the goal is to minimize the  
 443 cost function by reducing the absolute values of the feature coefficients. As a feature's  
 444 coefficient increases, so does the cost function value.

445 In other to find the best tuning parameter  $\lambda$ , according to procedures described by  
 446 Tibshirani (1996). Features were standardized in other to be mean centered (mean = 0) with unit  
 447 variance (standard deviation = 1), and split into training and test sets. Then 99 discrete  $\lambda$ -values  
 448 that range from 0.1 to 9.9 with a step of 0.1 ( $\lambda_1 = 0.1, \lambda_2 = 0.2, \lambda_3 = 0.3, \dots, \lambda_{99} = 9.9$ ) and 5-  
 449 fold cross-validation with a grid-search was applied to the training set. Which, randomly splits  
 450 all of the training set data up into 5 sets ( $y_1, y_2, y_3, y_4$  and  $y_5$ ), then LASSO minimization was  
 451 applied 5 times, each time fitted on 4 sets ( $y_1, y_2, y_3$  and  $y_4$ ) and tested on the hold-out set ( $y_5$ )  
 452 chosen randomly, to obtain the regression coefficients ( $\beta_i$ ) for a specific  $\lambda$ -value (for example  $\lambda_1$   
 453 = 0.1). The resulting coefficients, estimates the residuals values of the hold-out set ( $y_i$ ), and the  
 454 MSE (mean square error) was computed for each hold-out set ( $y_{i,i=1,\dots,5}$ ), defined by:

$$MSE = mean((y_i - \hat{y}_i)^2) \quad (4)$$

455 where  $y_i$  represents the response variable and  $\hat{y}_i$  is the residual. Then, the average of the MSE for  
 456 each  $y_{i,i=1,\dots,5}$ , was computed. The same procedure was repeated for the remaining 98  $\lambda$ -values,  
 457 generating a total number of 495 optimization iterations ( $99 \times 5$ ). After discovering the best  
 458 performing tuning parameter, the absolute values of the LASSO coefficients for each predictor  
 459 variables were obtained. Important features were selected ( $\beta_i > 0$ ) while, non-influential features  
 460 ( $\beta_i = 0$ ) were dropped. Finally, the features selected for Jiderebode, Lokoja and Niamey  
 461 watersheds are shown in Table 3.

462

463

464

465 **Table 3: Feature (Input) Combinations for LSTM Models for Selected Sub-catchments of**  
 466 **Niger River Basin**

Watershed	Input Combinations	Outputs
Lokoja	API, $P_{t-44}$ , $R_{82}$ , $T_{t-128}$ , $T_{m201}$	$Q_t$
Jiderebode	API, $P_{t-62}$ , $R_{194}$ , $T_t$ , $T_{t-130}$ , $T_{m230}$	$Q_t$
Niamey	API, $P_{t-119}$ , $R_{210}$ , $T_t$ , $T_{t-152}$ , $T_{m9}$	$Q_t$

467

### 468 2.4.3 Normal Quantile Transformations of Features

469 Hydrological and meteorological variables such as streamflow and precipitation are often  
 470 asymmetric, because these variables have positive values and range from 0 to  $\infty$ . There is also  
 471 the problem of seasonal variations, serial dependence and non-stationarity of the exogenous  
 472 variables of the time series. It is crucial to transform the distribution of hydrometeorological  
 473 variables and force them to follow a symmetric distribution, in order to satisfy the essential  
 474 assumption of normality, which represents a fundamental concept applicable to most statistical  
 475 and machine learning models (Moran, 1970; Goovaerts, 1997; Murphy, 2022). The Normal  
 476 Quantile Transform (NQT) has found extensive application in various hydrological and  
 477 meteorological contexts to perform nonlinear transformations of the Cumulative Distribution  
 478 Function (CDF) into the CDF of the Standard Normal Distribution (Moran, 1970; Bogner *et al.*,  
 479 2012), with its probability density function expressed as:

$$f_Y(y) = \frac{1}{\sqrt{2\pi\sigma^2}} e^{-\frac{1}{2}y^2} \quad (5)$$

480

481 In this study, the quantile-to-quantile normal score transformation was applied on each  
 482 feature independently to map the p-quantile of each feature data distribution to the p-quantile of  
 483 the standard normal distribution according to procedures described by Deutsch & Journal (1998);  
 484 Pyrcz & Deutsch (2018). Expressed as:

$$y = F_Y^{-1}(F_Z(z)) \quad \forall z \quad (6)$$

485

486 Where,  $z$  represents the feature with CDF  $F_Z(z)$ ,  $y$  is the normal score value with CDF  
 487  $F_Y(y)$  and  $F_Y^{-1}$  represents the Inverse CDF or quantile function of the output standard normal  
 488 distribution. The steps includes: Firstly, the feature is split into training set, validation set and test  
 489 set data; then the training set data is calibrated to generate the transformation parameters in order  
 490 to prevent leakage of information; the CDF of each feature in the feature space is estimated and  
 491 used to map the values of the observed variables to a uniform distribution; then, the associated  
 492 inverse CDF or quantile function ( $F_Y^{-1}$ ) is used to map the obtained values to the normal  
 493 distribution and; extreme values or outliers of the validation set and test set data that fall below  
 494 or above the fitted range of the training set data are mapped to the bounds of the output  
 495 distribution. NQT is a robust data preprocessing technique that smooths out datasets with  
 496 unusual distributions and is insensitive to outliers.

#### 497 2.4.4 Features and Target Normalization

498 The streamflow (target) daily time series of the hydrometric gauge stations were checked  
499 for missing data and, the missing data were filled by linear interpolation expressed as:

$$\hat{y} = y_1 + (x - x_i) \frac{(y_{i+1} - y_i)}{(x_{i+1} - x_i)} \quad (7)$$

500 where  $x_i$  and  $y_i$  represent the first coordinates, while  $x_{i+1}$  and  $y_{i+1}$  denote the second coordinates.  $x$   
501 represents the point at which interpolation is performed, and  $\hat{y}$  corresponds to the interpolated  
502 value.  
503

504 Most Deep Learning algorithms are not scale / shift invariant so it is important for the  
505 values of features and target to be within the same range. Transforming features and target to  
506 similar scale improves the performance of gradient descent, speeds up learning and, leads to  
507 faster convergence of the neural networks. Scaling is performed in other to prevent features with  
508 large values from dominating over small ones. Features (input variables) and targets  
509 (streamflow) were standardized in other to be mean centered with unit standard deviation. The  
510 procedures include: Firstly, the mean ( $\bar{x}$ ) and standard deviation ( $\sigma$ ) of the features and target of  
511 the training set were computed, as expressed by equations 8 – 9:

$$\bar{x} = \frac{1}{N} \sum_{i=1}^N x_i \quad (8)$$

$$\sigma = \sqrt{\frac{1}{N} \sum_{i=1}^N (x_i - \bar{x})^2} \quad (9)$$

512  
513 Then the training set, validation set and test set of both the features and target were scaled  
514 as expressed by the equation:

$$x'_i = \frac{x_i - \bar{x}}{\sigma} \quad (10)$$

515 where,  $\bar{x}$  and  $\sigma$  represents the mean and standard deviation of the variable  $x$ ,  $x_i$  represents the  
516 features and targets that are transformed (scaled) into  $x'_i$ .

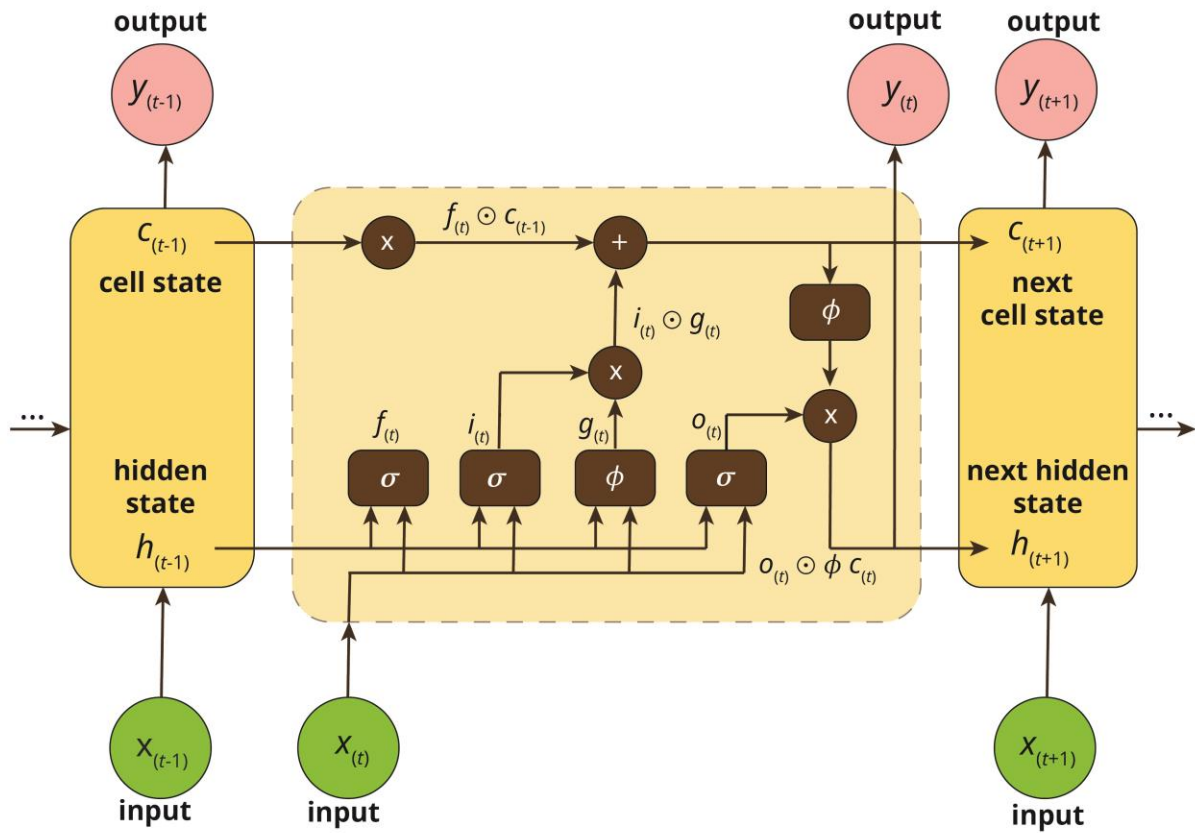
#### 517 2.5 Long short-term memory (LSTM)

518 Since the introduction of RNNs by William and Zipser in the late 1980s, RNNs and their  
519 variants have received a lot of research attention in recent times. RNN can capture nonlinear  
520 short-term temporal dependencies, in RNN architecture input sequences are mapped to a  
521 sequence of hidden states, which maps to an output. The success of RNN is hindered by the  
522 problem of vanishing and exploding gradients (Hochreiter & Schmidhuber, 1997), which reduces  
523 the ability to capture non-stationary long-term temporal dependencies.

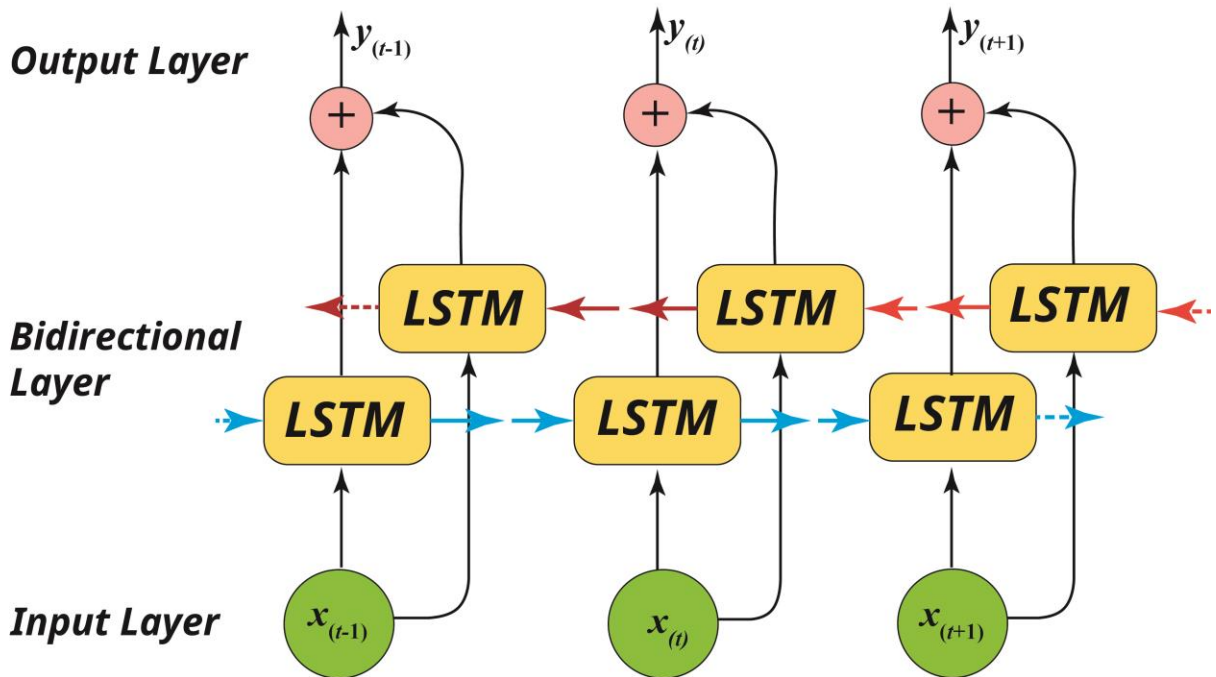
524 LSTM, displayed in Figure 3a, has the advantage over RNN to capture multiple non-  
525 stationary time dependencies and also long-term temporal dependencies due to the replacement  
526 of recurrent units in RNN with memory cells. LSTM cells consists of three gates: an input gate, a  
527 forget gate, and an output gate. These gates enable changes to be applied to a cell state vector  
528 and propagated iteratively in other to memorize and retrieve information over long time periods.  
529 The LSTM cell formulation are shown as follows:



(a)



(b)



530  
531  
532

Figure 3. (a) Architecture of a LSTM Unit; (b) Bidirectional LSTM Layer

533

$$\begin{aligned}
i_t &= \sigma(W_{xi}x_t + W_{hi}h_{t-1} + b_i) \\
f_t &= \sigma(W_{xf}x_t + W_{hf}h_{t-1} + b_f) \\
o_t &= \sigma(W_{xo}x_t + W_{ho}h_{t-1} + b_o) \\
g_t &= \phi(W_{xc}x_t + W_{hc}h_{t-1} + b_c) \\
c_t &= f_t \odot c_t + i_t \odot g_t \\
h_t &= o_t \odot \phi(c_t)
\end{aligned} \tag{11}$$

534

535 where  $i$  is the input gate,  $f$  is the forget gate and  $o$  is the output gate,  $c$  is the cell activation,  $g$  is  
536 the input modulation gate,  $h$  is the hidden vector; the term  $W$  and  $b$  represents the gate matrix and  
537 bias; while  $\phi$  represents a *tanh* function element-wise application and;  $\odot$  is the Hadamard  
538 product.

### 539 2.5.1 Bidirectional LSTM

540 Bidirectional LSTM networks, are cutting-edge neural network architectures, which  
541 integrate LSTM gating mechanisms with optimized cell state representations, which are  
542 propagated in both forward and reverse directions. Bidirectional LSTM, displayed in Figure 3b,  
543 takes into account dependencies in both time directions by including expected correlations in  
544 future time-steps and, as a result of reverse state propagation, anticipated future correlations can  
545 influence the current outputs of the network. Unlike RNN and unidirectional LSTM networks,  
546 bidirectional LSTMs have the capability to detect, store, extract and resolve with greater  
547 precision multidimensional temporal dependencies. This study utilized the Bidirectional LSTM  
548 capabilities in assessing the correlation between prior streamflow observations and future  
549 forecasts within the history window in resolving the current streamflow outputs.

### 550 2.5.2 LSTM Model Training

551 The Deep Learning (DL) method used for streamflow forecasting was Bidirectional  
552 LSTM. The models were trained in Python environment with TensorFlow v2 Deep Learning  
553 framework using NVIDIA Tesla K80, M60 and T4 GPUs (Graphics Processing Units).  
554 Catchment seasonality was explicitly represented in the Bidirectional-LSTM model formulation  
555 by transforming the feature matrix to tensors in the feature space, to provide a 90-day history  
556 window with 1-day horizon. The LSTM model architecture and hyperparameters considered for  
557 this study are presented in Tables 4 – 5. Input features and targets were split into three sets of  
558 data: training set; validation set and; test set. Inputs for Lokoja catchment were split into training  
559 set (2010 – 2017): validation set (2018 – 2020): test set (2021) while, Niamey catchment was  
560 split into training set (80 %): validation set (15 %): test set (5 %), and Jiderebode catchment was  
561 split into training set (80 %): validation set (10 %): test data (10 %). The LSTM models were  
562 trained with the training datasets while the validation datasets were used to generate the  
563 validation cost function (error function) for updating the weights of the neural networks during  
564 backpropagation and the test datasets was used to test model performance.

565

566

567

568

569

570

571

572 **Table 4: LSTM Model Architecture**

Layer type	Input layer	Output layer	Parameters
LSTM Bidirectional layer 1	90	300	186000
LSTM Bidirectional layer 2	300	100	140400
Dense layer 1	100	20	2020
Dropout		20 %	0
Dense layer 2	20	1	21
<b>Total Parameters</b>			<b>328441</b>

573

574

575 **Table 5: LSTM Model Hyperparameters**

Hyperparameters	Value
Evaluation interval	150
Activation function	Tanh
Optimizer	Adam
Loss function	Mean Squared Error (MSE)
Epoch	100
Monitor	Validation loss
Regularization	Dropout, Early stopping
Patience	10

576

## 2.6 Hydrological Model Evaluation Criteria

577

578

579

580

581

582

The performance of the LSTM and SWAT models were evaluated using NSE (Nash-Sutcliffe Efficiency), KGE (Kling Gupta Efficiency), KGE' (Adjusted Kling Gupta Efficiency), R<sup>2</sup> (Coefficient of Determination), RMSE (Root Mean Square Error) and PBIAS (percent of model bias).

KGE is expressed mathematically as:

$$KGE = 1 - \sqrt{(r - 1)^2 + \left[\left(\frac{\sigma_s}{\sigma_o}\right) - 1\right]^2 + \left[\left(\frac{\mu_s}{\mu_o}\right) - 1\right]^2} \quad (12)$$

583

584

585

where  $r$  represents the correlation coefficient between simulations and observations,  $\sigma$  represents the standard deviation,  $\mu$  denotes the mean, and the indices  $s$  and  $o$  correspond to the simulations and observation values, respectively. KGE ranges from  $-\infty$  to 1 (Gupta *et al.*, 2009).

586 The modified Kling Gupta Efficiency ( $KGE'$ ), the second objective function for  
587 evaluation of the performance of the hydrological models is expressed mathematically as:

$$KGE' = 1 - \sqrt{(r - 1)^2 + (\beta - 1)^2 + (\gamma - 1)^2} \quad (13)$$

588

589

590

$$\beta = \frac{\mu_s}{\mu_o}$$

$$\gamma = \frac{CV_s}{CV_o} = \frac{\sigma_s/\mu_s}{\sigma_o/\mu_o}$$

591

592 where  $KGE'$  represents the modified KGE-statistic,  $r$  represents the correlation coefficient  
593 between simulations and observations;  $b$  and  $\gamma$  are the bias ratio and variability ratio respectively;  
594  $\mu$  represents the mean,  $CV_s$  represents the coefficient of variation,  $\sigma$  represent the standard  
595 deviation, and the indices  $s$  and  $o$  corresponds to the simulations and observations respectively.  
596  $KGE'$  ranges from  $-\infty$  to 1 (Kling *et al.*, 2012).

597 The Nash-Sutcliffe Efficiency (NSE) serves as the third objective function for assessing  
598 the performance of the hydrological models is expressed mathematically as:

599

$$NSE = 1 - \left[ \frac{\sum_{i=1}^n (O_i - E_i)^2}{\sum_{i=1}^n (O_i - \bar{O})^2} \right] \quad (14)$$

600 where  $O_i$  represents the  $i$ -th observation of the variable under evaluation,  $E_i$  corresponds to the  $i$ -  
601 th simulation of the same variable,  $\bar{O}$  denotes the mean of the observed variables, and  $n$  signifies  
602 the total number of observations. NSE ranges from  $-\infty$  to 1 (Nash & Sutcliffe, 1970).

603 PBIAS, the fourth objective function for assessing the performance of the hydrological  
604 models is expressed mathematically as:

$$PBIAS = \frac{\sum_{i=1}^n (O_i - E_i) \times 100}{\sum_{i=1}^n (O_i)} \quad (15)$$

605 where  $O_i$  and  $E_i$  represents the  $i$ -th observation and simulation data respectively, and  $n$  represents  
606 the total number of observations. PBIAS ranges from  $-\infty$  to  $\infty$  (Gupta *et al.*, 1999).

607  $R^2$  (Coefficient of Determination), the fifth objective function for evaluation of the degree  
608 of collinearity between observations and simulated estimates is expressed mathematically as:

$$R^2 = \frac{[\sum_{i=1}^n (O_i - \bar{O}) \times (E_i - \bar{E})]^2}{[[\sum_{i=1}^n (O_i - \bar{O})^2]^{0.5} \times [\sum_{i=1}^n (E_i - \bar{E})^2]^{0.5}]^2} \quad (16)$$

609 where  $O_i$  and  $E_i$  are the  $i$ -th observation and simulation data respectively,  $\bar{O}$  is the mean of the  
610 observation,  $\bar{E}$  represent the mean of the simulation and  $n$  represents the total number of  
611 observations.  $R^2$  ranges from 0 to 1.

612 RMSE (root-mean square error), the sixth objective function for evaluation of the  
613 closeness of the simulated to observed streamflow is expressed mathematically as:

$$RMSE = \sqrt{\frac{\sum_{i=1}^n (O_i - E_i)^2}{n}} \quad (17)$$

614 where  $O_i$  and  $E_i$  are the  $i$ -th observation and simulation data respectively, and  $n$  represents the  
 615 total number of observations. RMSE ranges from 0 (perfect fit) to  $\infty$  (no fit) depending on the  
 616 relative range of the simulated to observed data.

617 Indicators of the best performing hydrological models are KGE, KGE', NSE and  $R^2$  of 1  
 618 and, PBIAS and RMSE of 0. These coefficients are used for assessment of the goodness of fit of  
 619 simulation and observed streamflow, and their performance rating is presented in Table 6.

620

621 **Table 6: Hydrological Model Metrics for Daily Time Series**

Performance Rating	NSE	KGE	KGE'	PBIAS (%)
Very good	$NSE \geq 0.7$	$KGE \geq 0.7$	$KGE' \geq 0.7$	$ PBIAS  \leq 25$
Good	$0.5 \leq NSE < 0.7$	$0.5 \leq KGE < 0.7$	$0.5 \leq KGE' < 0.7$	$25 <  PBIAS  \leq 50$
Satisfactory	$0.3 \leq NSE < 0.5$	$0.3 \leq KGE < 0.5$	$0.3 \leq KGE' < 0.5$	$50 <  PBIAS  \leq 70$
Unsatisfactory	$NSE < 0.3$	$KGE < 0.3$	$KGE' < 0.3$	$ PBIAS  > 70$

622

## 623 4 Results and Discussion

### 624 4.1 Results of Performances of NQT-API-LSTM and SWAT+ models

625 A comparison of the performances of SWAT+ and NQT-API-LSTM is shown in Table 7.  
 626 SWAT+ model showed very high efficiency at Lokoja watershed, the NSE values for calibration  
 627 was 0.71 and validation was 0.72, KGE values for calibration was 0.85 and validation was 0.81,  
 628 KGE' values for calibration was 0.85 and validation was 0.83, PBIAS values for calibration was  
 629 4.23 and validation was 8.74. The high values of the various efficiency criteria showed that  
 630 SWAT+ can be classified as a very good model and, suitable for accurately simulating daily  
 631 streamflow in large regional basins such as the Niger River Basin with regulated flows due to  
 632 presence of hydrological modifications such as Dams and Reservoirs.

633 NQT-API-LSTM models showed very high efficiency at Jiderebode, Lokoja and Niamey  
 634 watersheds. At Lokoja sub-catchment the values of NSE for calibration/training was 0.94,  
 635 validation was 0.93 and testing was 0.86, KGE for calibration/training was 0.96, validation was  
 636 0.85 and testing was 0.87, KGE' for calibration/training was 0.97, validation was 0.90 and testing  
 637 was 0.90 and PBIAS for calibration/training was -1.75, validation was 10.01 and testing was -  
 638 7.52. For Jiderebode watershed, the values of NSE for calibration/training was 0.81, validation  
 639 was 0.91 and testing was 0.89, KGE for calibration/training was 0.85, validation was 0.93 and  
 640 testing was 0.85, KGE' for calibration/training was 0.83, validation was 0.94 and testing was  
 641 0.90 and PBIAS for calibration/training was -11.81, validation was 2.76 and testing was 7.12.  
 642 While, Niamey sub-catchment, the values of NSE for calibration/training was 0.64, validation  
 643 was 0.82 and testing was 0.83, KGE for calibration/training was 0.73, validation was 0.90 and  
 644 testing was 0.83, KGE' for calibration/training was 0.69, validation was 0.91 and testing was  
 645 0.87 and PBIAS for calibration/training was -23.56, validation was -2.12 and testing was 5.35.

646

647

**Table 7: Streamflow Evaluation Metrics for LSTM and SWAT+ Model**

Streamflow	Model	Subbasin	NSE	KG <sub>E</sub> '	KG <sub>E</sub>	PBIAS (%)	R <sup>2</sup>	RMSE
Calibration/Training	SWAT+	Lokoja	0.71	0.85	0.85	4.23	0.71	3242.91
	Bi-LSTM	Lokoja	0.94	0.97	0.96	-1.75	0.94	1417.71
		Niamey	0.64	0.69	0.73	-23.56	0.64	374.10
		Jiderebode	0.81	0.83	0.85	-11.81	0.81	352.32
Validation	SWAT+	Lokoja	0.72	0.83	0.81	8.74	0.72	3762.55
	Bi-LSTM	Lokoja	0.93	0.90	0.85	10.01	0.93	1988.38
		Niamey	0.82	0.91	0.90	-2.12	0.82	261.04
		Jiderebode	0.91	0.94	0.93	2.76	0.91	280.44
Testing	Bi-LSTM	Lokoja	0.86	0.90	0.87	-7.52	0.86	1994.96
		Niamey	0.83	0.87	0.83	5.35	0.83	319.91
		Jiderebode	0.89	0.90	0.85	7.12	0.89	349.64

648

649

650

651

652

653

654

655

656

657

658

659

660

661

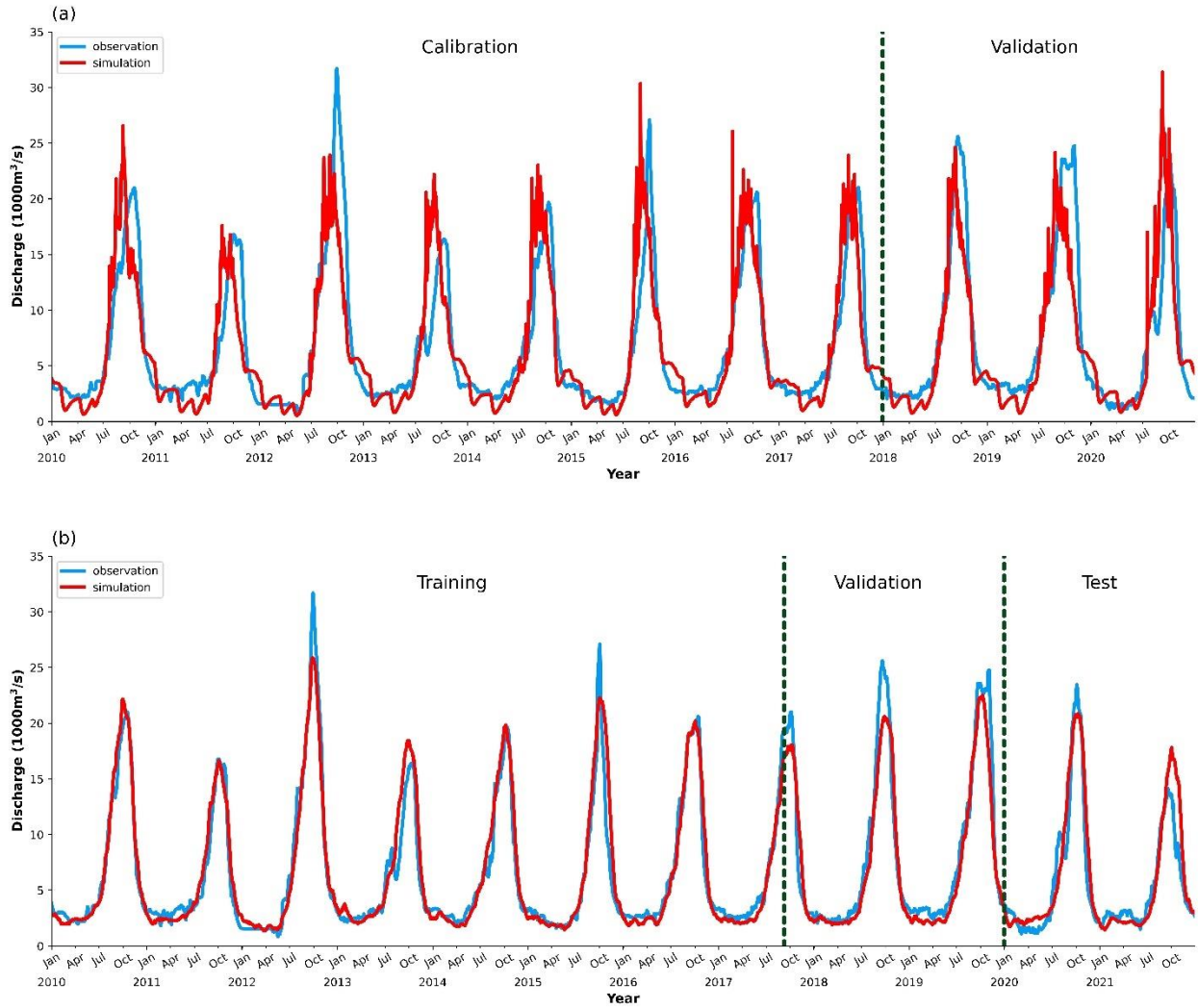
662

663

664

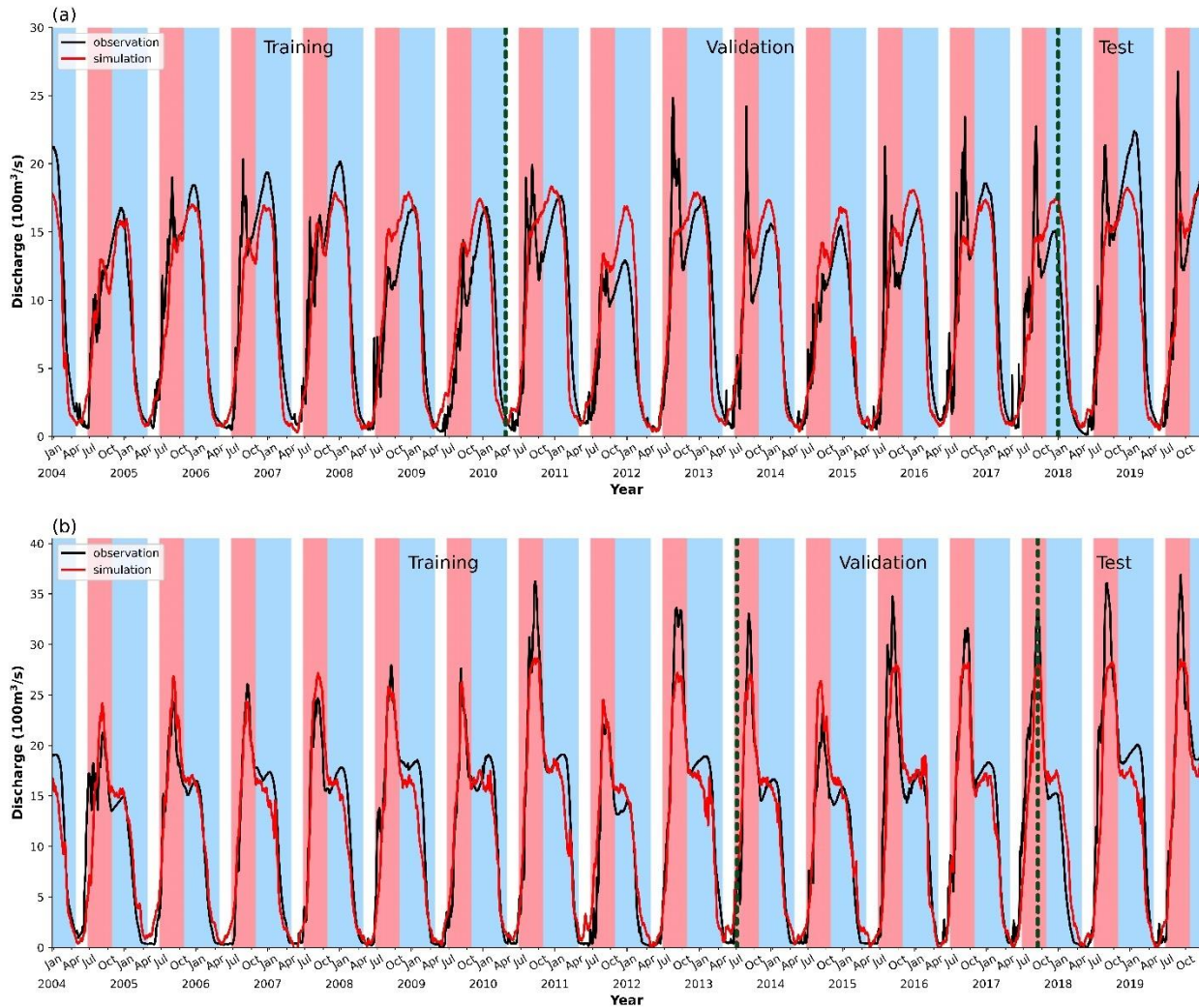
The high performance of NQT-API-LSTMs at all sub-catchments (Jiderebode, Lokoja, Niamey) also showed that NQT-API-LSTM can be classified as very good models for simulating and forecasting daily streamflow in large regional basins with heterogeneous climatic, topographic and geological conditions. Also, NQT-API-LSTM outperformed SWAT+ model and exhibited expert skills in predicting the influence of regulated upstream flows in downstream catchments of the basin, due to presence of dams and the hydrological settings of the Inland Delta.

The hydrographs of simulated and observed daily streamflow characteristics by SWAT model for the period 2010 to 2020 and NQT-API-LSTM models for the period 2010 to 2021 for Lokoja gauging station is shown in Figure 3 while, a subset of the simulated and observed daily streamflow characteristics for Jiderebode and Niamey gauging stations simulated by NQT-API-LSTM models for the period 2010 to 2019 is displayed in Figure 4. The daily simulated streamflow hydrograph at Lokoja station of NRB showed that SWAT model underestimated low flows, overestimated peak flows slightly, and observed peak flow lagged behind the simulated peak flow. NQT-API-LSTM was able to capture the underlying streamflow behaviour and pattern more accurately, and showed superior performance in estimating low flow but



665  
 666 Figure 4: Hydrograph of Simulated Streamflow at Lokoja gauging station for the period 2010 to  
 667 2020: (a) SWAT model; (b) NQT-API-LSTM.  
 668

669  
 670  
 671  
 672  
 673  
 674



675  
 676 Figure 5: Hydrograph of NQT-API-LSTM Simulated Streamflow for the period 2004 to 2019:  
 677 (a) Niamey station, Sahelian flooding depicted in red while Guinean flooding is indicated in  
 678 blue; (b) Jiderebode station, Sudan flooding depicted in red, and Guinean flooding is indicated in  
 679 blue.

680  
 681 underestimated peak flow slightly at Lokoja watershed. NQT-API-LSTM ensemble showed very  
 682 high performance in simulating the streamflow pattern at Jiderebode sub-catchment, and showed  
 683 very good skills in estimating low flow but underestimated peak flow. The NQT-API-LSTM  
 684 model displayed expert skills in simulating the two flood events at Jiderebode station which  
 685 include: the Guinean Flood (black flood) and; the Sudan Flood (white flood). The NQT-API-  
 686 LSTM underestimated the white flood peak but showed better performance in simulating the  
 687 black flood peak at Jiderebode sub-catchment. NQT-API-LSTM showed very good skills in  
 688 simulating the streamflow pattern of the black flood and red flood events at Niamey sub-  
 689 catchment, and also showed very good performance in estimating low flow. The NQT-API-  
 690 LSTM underestimated the Sahelian peak (red flood) but showed better performance in  
 691 simulating the Guinean peak (black flood) at Niamey sub-catchment.



## 692 4.2 Discussion

693 Generally, SWAT+ and NQT-API-LSTM models accurately reproduced the streamflow,  
694 with the SWAT+ model slightly overestimating peak flows. It has been reported that SWAT+  
695 model's peak-flow inefficiency may be attributed to model formulation (Jimeno-Sáez et al,  
696 2018). However, NQT-API-LSTM ensemble estimations were more accurate and closely  
697 matched the observed streamflow, which was reflected in the lower RMSE in  
698 calibration/training, validation and test phases. The varying performance of NQT-API-LSTMs  
699 across the various gauging stations may be attributed to differences in surface and extremely  
700 heterogenous climatic conditions from the hyper-arid region of Sahara Desert at the Northern  
701 NRB to the humid region of the Guinean Niger Basin at Lokoja. The observed and simulated  
702 discharge ( $> 2000 \text{ m}^3/\text{s}$ ) during the dry season, provide additional evidence of a link between  
703 groundwater return flow and streamflow, and would suggest that "Variable Source Areas  
704 Concept" is applicable at Lokoja catchment, hence the success of NQT-API-LSTM ensemble. In  
705 addition, there was also influence of regulated flows from more than 260 Dams and Reservoirs  
706 within the upstream sections of the basin. However, due to data limitations and model  
707 complexity, management or decision variables (such as reservoir storage, release schedule,  
708 volume, principal and emergency spillway as well as irrigation extraction rates) were not  
709 included in NQT-API-LSTM model formulation.

710 A cursory glance at Figure 3 reveals a very good fit, and identical pattern of both  
711 simulated and observed streamflow in all phases of the hydrograph at Lokoja sub-catchment,  
712 which underscores the efficacy of NQT-API-LSTMs in learning the causal relationships of the  
713 climatic drivers influencing streamflow in the watershed. An additional reason for the better  
714 performance of NQT-API-LSTM model at Lokoja watershed may be attributed to the surface  
715 attributes and humid climatic condition. Discharge of rivers in humid regions are less sensitive to  
716 climate input due to higher runoff and lower infiltration rate. The results showed that NQT-API-  
717 LSTM can help reduce streamflow overestimation which was inherent in SWAT+ model,  
718 although it was slightly underestimated by NQT-API-LSTM. Machine learning models tends to  
719 predict values closer to the mean of the distribution better than values at the extremes (high and  
720 lows). A possible reason for this discrepancy might be that peaks with high values are scarce,  
721 when compared with values of average peaks in the training data sets, and the LSTM model  
722 assigns relatively more importance to the average values rather than the high values extremes.  
723 These findings suggest a need for extreme caution in applying NQT-API-LSTMs for  
724 extrapolating beyond the bounds of the historically observed training data range, especially in  
725 anomaly detection and studies on extreme flood events. Results obtained by Jimeno-Sáez et al.  
726 (2018); Minns & Hall (1996) are consistent with our findings. The rolling total rainfall ( $R_n$ ) and  
727 API, a proxy for catchment wetness, accounts for infiltration and groundwater dynamics at  
728 watershed-scale. Considering the remarkably strong regional heterogeneity in rainfall  
729 distribution, temperature dynamics, aridity and surface properties across the structure of the  
730 basin. NQT-API-LSTM ensemble outshined with its simplified ability to approximate the  
731 streamflow at the arid (Niamey), semi-arid (Jiderebode) and humid (Lokoja) environments.

732 Though, input data acquisition (such as meteorological variables) and, preprocessing is  
733 comparatively easier for NQT-API-LSTMs, the limitations of both NQT-API-LSTMs and  
734 SWAT+ for basin-scale modeling framework are increasingly apparent. The study basin is very  
735 large and sparsely gauged, which significantly increases the difficulty in acquiring the necessary  
736 meteorological and topography data to parameterize a physically-based model. In addition, the  
737 setup and calibration for SWAT+ model is computationally more expensive and takes

738 considerably more time than NQT-API-LSTM. Conversely, obtaining a consistent timeseries of  
739 in-situ meteorological and hydrological data to calibrate a data-driven model is very challenging  
740 in West Africa. Since, the study area is a large regional basin, watershed delineation, data  
741 preprocessing and spatial averaging of meteorological variables incurs additional computational  
742 cost. NQT-API-LSTMs function as black-box models, and they do not provide information on  
743 the water balance and its constituent components. However, relying solely on precipitation and  
744 temperature as input variables for the models, represents a constraint in the case of NQT-API-  
745 LSTM ensemble because the interaction between rainfall and runoff is influenced by various  
746 biophysical parameters. Which confers an advantage to SWAT+ when exploring a number of  
747 scenarios concerning the basin's response to land use and land management. The general picture  
748 emerging from the results of this study is that both SWAT+ and NQT-API-LSTM models are  
749 suitable for simulating streamflow in large basins. However, it is recommended to use NQT-  
750 API-LSTMs for studies on extreme hydrologic events (such as floods), hydrological  
751 management (low-flow events) and developing scenarios for climate change impact on the  
752 hydrological processes. While, SWAT+ model is advisable for assessing the hydrological  
753 response of the watershed to land use/land cover (LULC) changes.

754 NQT-API-LSTM was able to capture the Guinean and Sahelian flood events at Niamey  
755 station however, the Guinean Flood was more accurately reproduced than the Sahelian Flood.  
756 These findings are less surprising if we consider the strong influence of the headwaters of the  
757 Niger River from the humid Guineo-Congolian region in Guinea, associated with higher runoff  
758 and lower infiltration rate on one hand and, the hydrological settings within the vast wetlands of  
759 the Inland Delta, leading to delay in arrival of the black flood at Niamey. This can be explained  
760 by the 90-day history window, which enabled NQT-API-LSTM to effectively understand the  
761 seasonal correlation between historical and future streamflow patterns while, considering the 3-  
762 month streamflow delay due to groundwater recharge in the aquifer system of the Inland Delta.  
763 The results confirm the findings of Aich et al. (2014), which posits that the hydrological  
764 conditions in the upstream region of the Sahelian NRB significantly influence the Guinean  
765 Flood. However, the Sahelian flooding has a shorter duration with inconsistent Peak flow that is  
766 not easily identified in some years thus, making it difficult for NQT-API-LSTM to learn its  
767 distribution and, therefore assign relatively more importance to the Guinean flood. An additional  
768 reason for lower accuracy in predicting the Sahelian flooding may be attributed to increased  
769 complexity in modeling the hydrological responses of arid and semi-arid regions, which are more  
770 sensitive to climate inputs, due to high infiltration and evapotranspiration rates and also limited  
771 and / or irregular precipitation. There are also uncertainties in the meteorological reanalysis  
772 whose deficiency could most easily reflect on the model's performance in arid and semi-arid  
773 regions.

774 NQT-API-LSTM was also able to capture both the Guinean and Sudan Flood events at  
775 Jiderebode station, but reproduced the Sudan Flood (white flood) more accurately than the  
776 Guinean Flood (black flood). A possible reason for this discrepancy might be that the delayed  
777 arrival of the black flood at Jiderebode in the dry season due to hydrometeorological dynamics at  
778 the Inland Delta and the upstream Sahelian basin constituted additional difficulty for the model.  
779 It might seem counterintuitive that NQT-API-LSTM ensemble reproduced the white flood more  
780 accurately than the black flood at Jiderebode station, but considering the fact that the white flood  
781 occurs during the wet season due to surface runoff and groundwater dynamics. NQT-API-LSTM  
782 was able to capture the influence of seasonal climate, catchment seasonality and wetness on  
783 monsoon streamflow. In Seasonal climates, increased rainfall during the wet season, followed by

784 recharge and increased groundwater storage, results to elevated increase in the regional water  
785 table, which is seasonally dynamic and may vary in relation to rainfall variation and its climatic  
786 drivers (Davie & Quinn, 2019). An interesting side finding was that precipitation within the  
787 Saharan region was indirectly influencing the downstream flow at the Sudan region through the  
788 Continental Terminal of the Iullemeden. Since, the data preprocessing was applied to the entire  
789 upstream catchment from the Saharan to the Sudan regions of the basin. NQT-API-LSTM was  
790 able to learn the synergistic contributions of all climatic regions to streamflow. Overall, results of  
791 this study provide support for the validity of NQT-API-LSTM approach for simulating and  
792 forecasting streamflow in large watersheds due to its simplified model formulation requiring  
793 only meteorological variables and minimal computational resources, with the possibilities of  
794 exploring other hydrological processes including water quality and water levels, as reported in  
795 some studies (Chen et al., 2022; Cho et al., 2023; Pyo et al., 2023; Vizi et al., 2023).  
796

## 797 **5 Conclusions**

798 In this study, we proposed a novel framework; a climate data-driven NQT-API-LSTM  
799 ensemble, and compared the performance with SWAT+, a quasi-physically based model, for  
800 daily streamflow forecasting. To validate their competency, they were applied in NRB, the  
801 largest transboundary river basin in West Africa, consisting of hyper-arid, arid, semi-arid, dry-  
802 subhumid and humid climatic conditions. The combination of API and LSTM for multivariate  
803 time series forecasting leverage on the synergy of API and deep learning techniques in surface  
804 water modeling. This approach exploits LSTMs sophisticated capability to capture complex  
805 temporal and seasonal dependencies while taking into consideration the inherent strengths of API  
806 in estimating catchment wetness, particularly in NRB where streamflow is strongly influenced  
807 by soil water or groundwater. The rolling total rainfall ( $R_n$ ) also accounted for catchment wetness  
808 while, LASSO was used for selection of input variables which was transformed to a Gaussian  
809 distribution using NQT. The SWAT+ model was calibrated with daily streamflow observations  
810 using the Latin hypercube algorithm. The results indicated that NQT-API-LSTM ensemble  
811 showed better performance in simulating streamflow at Lokoja watershed and was able to  
812 reproduce the influence of rainfall and temperature variations and its climatic drivers adequately.  
813 While LSTM approach was superior to SWAT+ methods as shown in this study, SWAT+ can be  
814 used as an alternative hydrological model, especially to assess the basin's response to land  
815 use/land cover changes. In light of the very good performance of NQT-API-LSTM, few  
816 conclusions can be drawn from the results of this study: Streamflow at the Middle and Lower  
817 Niger River Basin is heavily influenced by climate and regional groundwater dynamics at the  
818 upstream sections of the basin; the Saharan section of the basin is hydrologically active and its  
819 rainfall and temperature variations influences the seasonal dynamics of the regional groundwater  
820 table; the Black Flood was more accurately reproduced than the Red Flood at Niamey; the White  
821 Flood was simulated with greater precision than the Black Flood at Jiderebode; the model was  
822 able to predict regulated flows accurately in downstream catchments and; NQT-API-LSTM is  
823 suitable for studies on extreme events (such as floods), hydrological management (low flow  
824 events e.g. hydropower generation) and climate change impact on hydrological processes. The  
825 major advantages of the NQT-API-LSTMs are its ability to learn the basin's response to climate  
826 change and variability remotely, without the need for spatially-explicit biophysical  
827 characteristics of the watershed. In this study, only precipitation and temperature inputs were  
828 considered. Therefore, the current study could be improved by including additional input

829 variables that influences streamflow and, exploring the neural search space to discover more  
830 sophisticated deep learning architectures and hyperparameters.  
831

## 832 **Acknowledgments**

833 This work was supported by the Microsoft AI4Earth Grant by providing Microsoft Azure Credits  
834 for access to computational resources hosted on Microsoft Azure Cloud Computing Services,  
835 and access to Microsoft Planetary Computer. Microsoft AI4Earth Team also supported with  
836 training, mentorship and provision of curated codes from open sources for the Cloud Native  
837 Geospatial Data Analysis and Deep Learning workflow. The first author was supported by the  
838 Nigerian Hydrological Services Agency (NiHSA) and the Upper Niger River Basin  
839 Development Authority (UNRBDA). The first author is grateful to ESRI for the ArcGIS Pro  
840 Professional Advanced User software license grant.

841  
842

## 843 **Data Availability Statement**

844 The observed streamflow data for Jiderebode and Lokoja stations are confidential, and the  
845 authors do not have permission to share the data. ArcGIS Pro software would require the  
846 purchase of a license (<https://www.esri.com/en-us/arcgis/products/arcgis-pro/buy#for-business> ).  
847 All other data analyzed in this study are from open sources and publicly available. River  
848 discharge data for Niamey station (GRDC, 2024), HydroSHEDS hydrologically conditioned  
849 DEM (Lehner et al., 2008; Lehner, 2022) is available at  
850 ([https://data.hydrosheds.org/file/hydrosheds-v1-con/af\\_con\\_3s.zip](https://data.hydrosheds.org/file/hydrosheds-v1-con/af_con_3s.zip) ), HWSD soil data (FAO,  
851 2012), ESA WorldCover 10 m 2020 v100 (Zanaga et al., 2021) is available at Microsoft  
852 Planetary Computer (Microsoft Open Source et al., 2022), ERA5 reanalysis climate data  
853 (Muñoz, 2019) is also available at Microsoft Planetary Computer (Microsoft Open Source et al.,  
854 2022), HyBAS HydroBasins (Lehner and Grill, 2013) is available at  
855 ([https://data.hydrosheds.org/file/hydrobasins/standard/hybas\\_af\\_lev01-12\\_v1c.zip](https://data.hydrosheds.org/file/hydrobasins/standard/hybas_af_lev01-12_v1c.zip) ),  
856 HydroSHEDS HydroLAKES (<https://www.hydrosheds.org/products/hydrolakes/> ), SWAT+  
857 model (<https://swat.tamu.edu/software/plus/> ), SWAT+ Toolbox  
858 (<https://swat.tamu.edu/software/plus/> ) and QGIS  
859 (<https://www.qgis.org/en/site/forusers/download.html> ).

860

861

## 862 **References**

863 Adeogun, A. G., Ibitoye, B. A., Salami, A. W., & Ihagh, G. T. (2018). Sustainable management  
864 of erosion prone areas of upper watershed of Kainji hydropower dam, Nigeria. *Journal of King*

- 865 *Saud University – Engineering Sciences*, 32(1): 5–10.
- 866 <https://doi.org/10.1016/j.jksues.2018.05.001>
- 867 Aich, V., Liersch, S., Vetter, T., Andersson, J. C. M., Müller, E. N. & Hattermann, F. F. (2015).
- 868 Climate or Land Use?—Attribution of Changes in River Flooding in the Sahel Zone. *Water*, 7,
- 869 2796–2820, <https://doi.org/10.3390/w7062796>
- 870 Ali, S., Ghosh, N. C., & Singh, R. (2010). Rainfall–runoff simulation using a normalized
- 871 antecedent precipitation index. *Hydrological Sciences Journal – Journal des Sciences*
- 872 *Hydrologiques*, 55(2), 266–274, <http://dx.doi.org/10.1080/02626660903546175>
- 873 Amirhossien, F., Alireza, F. Kazem, J., & Mohammadbagher, S. (2015). A Comparison of ANN
- 874 and HSPF Models for Runoff Simulation in Balkhichai River Watershed, Iran. *American Journal*
- 875 *of Climate Change*, 4, 203–216, <https://dx.doi.org/10.4236/ajcc.2015.43016>
- 876 Andersen, I., Dione, O., Jarosewich-holder, M., Olivry, J.-C., & Golitzen, K. G. (2005). The
- 877 Niger River Basin: A Vision for Sustainable Management. *The International Bank for*
- 878 *Reconstruction and Development / The World Bank*. <https://doi.org/10.1596/978-0-8213-6203-7>
- 879 Arnold, J. G., Srinivasan, R., Mutiah, R. S., & Williams, J. R. (1998). Large area hydrologic
- 880 modeling and assessment part I: model development, *JAWRA Journal of the American Water*
- 881 *Resources Association*, 34(1):73–89. <https://doi.org/10.1111/j.1752-1688.1998.tb05961.x>
- 882 Arnold, J. G., Moriasi, D. N., Gassman, P. W., Abbaspour, K. C., White, M. J., Srinivasan, R., et
- 883 al. (2012). SWAT: Model use, calibration, and validation. *Transactions of the ASABE*, 55, 1491–
- 884 1508. <https://doi.org/10.13031/2013.42256> @2012
- 885 Awchi, T. A. (2014). River discharges forecasting in Northern Iraq using different ANN
- 886 techniques. *Water Resources Management*, 28(3), 801–814. [https://doi.org/10.1007/s11269-014-](https://doi.org/10.1007/s11269-014-0516-3)
- 887 0516-3

- 888 Bieger, K., Arnold, J. G., Rathjens, H., White, M. J., Bosch, D. D., Allen, P. M., et al. (2017).  
889 Introduction to SWAT+, Introduction to SWAT+, A Completely Restructured Version of the  
890 Soil and Water Assessment Tool. *Journal of the American Water Resources Association*  
891 (*JAWRA*), 53(1), 115–130. <https://doi.org/10.1111/1752-1688.12482>
- 892 Bogner, K., Pappenberger, F., & Cloke, H. L. (2012). Technical Note: The normal quantile  
893 transformation and its application in a flood forecasting system. *Hydrology and Earth System*  
894 *Sciences*, 16, 1085–1094. <https://doi.org/10.5194/hess-16-1085-2012>.
- 895 Borah, D. K., Yagow, G., Saleh, A., Barnes, P. L., Rosenthal, W., Krug, E. C., & Hauck, L. M.  
896 (2006). Sediment and nutrient modeling for TMDL development and implementation.  
897 *Transactions of the ASABE*, 49(4): 967–986. <https://doi.org/10.13031/2013.21742> @2006
- 898 Chen, H., Yang, J., Fu, X., Zheng, Q., Song, X., Fu, Z., et al. (2022). Water Quality Prediction  
899 Based on LSTM and Attention Mechanism: A Case Study of the Burnett River, Australia.  
900 *Sustainability*, 14, 13231. <https://doi.org/10.3390/su142013231>.
- 901 Cho, M., Kim, C., Jung, K., & Jung, H. (2023). Water Level Prediction Model Applying a Long  
902 Short-Term Memory (LSTM)–Gated Recurrent Unit (GRU) Method for Flood Prediction. *Water*,  
903 14, 2221. <https://doi.org/10.3390/w14142221>.
- 904 d'Herbès, J. M., & Valentin, C. (1997). Land surface conditions of the Niamey region: ecological  
905 and hydrological implications. *Journal of Hydrology*, 188–189, 18–42.  
906 [https://doi.org/10.1016/S0022-1694\(96\)03153-8](https://doi.org/10.1016/S0022-1694(96)03153-8)
- 907 Danandeh M. A. (2018). An improved gene expression programming model for streamflow  
908 forecasting in intermittent streams. *Journal of Hydrology*, 563, 669–678.  
909 <https://doi.org/10.1016/j.jhydrol.2018.06.049>

- 910 Duan, Q., Pappenberger, F., Wood, A., Cloke, H. L., & Schaake, J. C. (2019). Handbook of  
911 Hydrometeorological Ensemble Forecasting. *Springer, Berlin, Heidelberg*.  
912 <https://doi.org/10.1007/978-3-642-40457-3>
- 913 Davie, T., & Quinn, N. W. (2019). Fundamentals of hydrology, 3rd Eds, *Routledge*, ISBN  
914 9780415858694. <https://lcn.loc.gov/2018057141>
- 915 Dawson, C. W., & Abrahart, R. J. (2007). Evaluation of two different methods for the antecedent  
916 precipitation index in neural network river stage forecasting. *Geophysical Research Abstracts*, 9,  
917 07522.
- 918 Demirel, M. C., Venancio, A., & Kahya, E. (2009). Flow forecast by SWAT model and ANN in  
919 Pracana Basin, Portugal. *Advances in Engineering Software*, 40, 467–473.  
920 <https://doi.org/10.1016/j.advengsoft.2008.08.002>
- 921 Descroix, L., Genthon, P., Amogu, O., Rajot, J.-L., Sighomnou, D., & Vauclin, M. (2012).  
922 Change in Sahelian rivers hydrograph: the case of recent red floods of the Niger River in the  
923 Niamey region. *Global and Planetary Change*, 98–99, 18–30.  
924 <http://dx.doi.org/10.1016/j.gloplacha.2012.07.009>
- 925 Descroix, L., Nouvelot, J. F., & Vauclin, M. (2002). Evaluation of an antecedent index to model  
926 runoff yield in the western Sierra Madre (north-west Mexico). *Journal of Hydrology*, 263, 114–  
927 130. [https://doi.org/10.1016/S0022-1694\(02\)00047-1](https://doi.org/10.1016/S0022-1694(02)00047-1)
- 928 Deutsch, C. V., & Journel, A. G. (1998). GSLIB: Geostatistical Software Library and User  
929 Guide, 2nd Ed., *Oxford University Press*, USA.
- 930 FAO/IIASA/ISRIC/ISS-CAS/JRC (2012). Harmonized World Soil Database (Version 1.2);  
931 *FAO*: Rome, Italy; *IIASA*: Laxenburg, Austria, 2012; Available online:

932 <https://www.fao.org/soils-portal/data-hub/soil-maps-and-databases/harmonized-world-soil->  
933 [database-v12/en/](https://www.fao.org/soils-portal/data-hub/soil-maps-and-databases/harmonized-world-soil-database-v12/en/) (accessed on 15 March 2023).

934 Fontes, J.-C., Andrews, J. N., Edmunds, W. M., Guerre, A., & Travi, Y. (1991). Paleorecharge  
935 by the Niger River (Mali) Deduced from groundwater geochemistry. *Water Resources Research*,  
936 27(2), 199–214. <https://doi.org/10.1029/90wr01703>

937 Fryirs, K. A., & Brierley, G. J. (2013). River Behaviour. In *Geomorphic Analysis of River*  
938 *Systems* (eds K. A. Fryirs and G. J. Brierley). Wiley-Blackwell.  
939 <https://doi.org/10.1002/9781118305454.ch11>

940 Fu, M., Fan, T., Ding, Z., Salih, S. Q., Al-Ansari, N., & Yaseen, Z. M. (2020). Deep Learning  
941 Data-Intelligence Model Based on Adjusted Forecasting Window Scale: Application in Daily  
942 Streamflow Simulation. *IEEEAccess*, 8: 32632–32651.  
943 <https://doi.org/10.1109/ACCESS.2020.2974406>

944 Ghorbani, M. A., Khatibi, R., Goel, A., FazeliFard, M. H., & Azani, A. (2016). Modeling River  
945 Discharge Time Series using Support Vector Machine and Artificial Neural Networks.  
946 *Environmental Earth Sciences*, 75(8) 685. <https://doi.org/10.1007/s12665-016-5435-6>

947 Ghosh, N. C., Jaiswal, R. K., & Ali, S. (2021). Normalized Antecedent Precipitation Index Based  
948 Model for Prediction of Runoff from Un-Gauged Catchments. *Water Resources Management*,  
949 35, 1211–1230. <https://doi.org/10.1007/s11269-021-02775-w>

950 Goovaerts, P. (1997). Geostatistics for Natural Resources Evaluation, *Applied Geostatistics*  
951 *Series*, Oxford University Press, USA. <https://doi.org/10.1093/oso/9780195115383.001.0001>

952 GRDC. (2024). The Global Runoff Data Centre, 56068 Koblenz, Germany. Available online:  
953 <https://portal.grdc.bafg.de/applications/public.html?publicuser=PublicUser#dataDownload/Home>  
954 / (accessed on 8 April 2024).



- 955 Grusson, Y., Anctil, F., Sauvage, S., & Sánchez Pérez, J. M. (2017). Testing the SWAT Model  
956 with Gridded Weather Data of Different Spatial Resolutions. *Water*, 9(1), 54.  
957 <https://doi.org/10.3390/w9010054>
- 958 Guo, J., Zhou, J., Qin, H., Zou, Q., & Li, Q. (2011). Monthly Streamflow Forecasting Based on  
959 Improved Support Vector Machine Model. *Expert Systems with Applications*, 38(10): 13073–  
960 13081. <https://doi.org/10.1016/j.eswa.2011.04.114>
- 961 Gupta, H. V., Kling, H., Yilmaz, K. K., & Martinez, G. F. (2009). Decomposition of the mean  
962 squared error and NSE performance criteria: Implications for improving hydrological modelling.  
963 *Journal of Hydrology*, 377, 80–91. <https://doi.org/10.1016/j.jhydrol.2009.08.003>
- 964 Gupta, H. V., Sorooshian, S., & Yapo, P. O. (1999). Status of Automatic Calibration for  
965 Hydrologic Models: Comparison with Multilevel Expert Calibration. *Journal of Hydrologic  
966 Engineering*, 4, 135–143. [https://doi.org/10.1061/\(ASCE\)1084-0699\(1999\)4:2\(135\)](https://doi.org/10.1061/(ASCE)1084-0699(1999)4:2(135))
- 967 Haykin S. (1999). *Neural Networks. A Comprehensive Foundation*, 2nd Edition. Prentice Hall  
968 PTR, Englewood Cliffs, New Jersey, USA, ISBN 0132733501. pp 696.
- 969 Heggen, R. J. (2001). Normalized antecedent precipitation index. *Journal of Hydrologic  
970 Engineering ASCE*, 6(5), 377–381. [https://doi.org/10.1061/\(ASCE\)1084-0699\(2001\)6:5\(377\)](https://doi.org/10.1061/(ASCE)1084-0699(2001)6:5(377))
- 971 Hochreiter, S., & Schmidhuber, J. (1997). Long short-term memory. *Neural Computation*, 9(8),  
972 1735-1780. <https://doi.org/10.1162/neco.1997.9.8.1735>
- 973 Hewlett, J. D. and Hibbert, A. R. (1967). Factors affecting the response of small watershed to  
974 precipitation in humid areas. In: W. E. Soper and H. W. Lull(eds.), *International Symposium on  
975 Forest Hydrology*, Pengamonb, Oxford, 275-290.

- 976 Hussain, D., Hussain, T., Khan, A. A., Naqvi, S. A. A., & Jamil, A. (2020). A deep learning  
977 approach for hydrological time-series prediction: A case study of Gilgit river basin. *Earth  
978 Science Informatics*, 13:915–927. <https://doi.org/10.1007/s12145-020-00477-2>
- 979 IAEA (2017). Iullemeden Aquifer System: Report of the IAEA-Supported Regional Technical  
980 Cooperation Project RAF/7/011. Integrated and Sustainable Management of Shared Aquifer  
981 Systems and Basins of the Sahel Region. IAEA, Vienna, Austria, 2017.
- 982 Jha, M. K., Gassman, P. W., & Arnold, J. G. (2007). Water Quality Modeling for the Raccoon  
983 River Watershed using SWAT. *Trans. ASABE*, 50(2), 479–493.  
984 <https://doi.org/10.13031/2013.22660>
- 985 Jimeno-Sáez, P., Senent-Aparicio, J., Pérez-Sánchez, J., & Pulido-Velazquez, D. (2018). A  
986 Comparison of SWAT and ANN Models for Daily Runoff Simulation in Different Climatic  
987 Zones of Peninsular Spain. *Water*, 10(192), 1–19, <https://dx.doi.org/10.3390/w10020192>
- 988 Jimoh, O. D. (2007). Impacts of Dams on the Hydrology of River Niger at Lokoja, Nigeria. *Arid  
989 Zone Journal of Engineering, Technology and Environment*, 5: 1–12.
- 990 Kling, H., Fuchs, M., & Paulin, M. (2012). Runoff conditions in the upper Danube basin under  
991 an ensemble of climate change scenarios. *Journal of Hydrology*, 422–425, 264–277.  
992 <https://doi.org/10.1016/j.jhydrol.2012.01.011>
- 993 Kohler, M. A., & Linsley, R. K. (1951). Predicting the Runoff from Storm Rainfall, U.S.  
994 *Weather Bureau Research Paper*. No. 34.
- 995 Lehner, B. (2022). HydroSHEDS Technical Documentation Version 1.4; *World Wildlife Fund  
996 US*: Washington, DC 20037, USA.
- 997 Lehner, B., Verdin, K., & Jarvis, A. (2008). New global hydrography derived from spaceborne  
998 elevation data. *Eos, Transactions*, 89(10), 93–94. <https://doi.org/10.1029/2008EO100001>

- 999 Lehner, B., & Grill G. (2013). Global River Hydrography and Network Routing: Baseline Data  
1000 and New Approaches to Study the World's Large River Systems. *Hydrological Processes*,  
1001 27(15), 2171–2186. <https://doi.org/10.1002/hyp.9740>
- 1002 Lehner, M. L., Grill, B., Nedeva, G., & Schmitt, I. O. (2016). Estimating the volume and age of  
1003 water stored in global lakes using a geo-statistical approach. *Nature Communications*, 7, 13603.  
1004 <https://doi.org/10.1038/ncomms13603>
- 1005 Lienou, G., Mahe, G., Dieulin, C., Paturel, J. E., Bamba, F., Sighomnou, D., & Dessouassi, R.  
1006 (2010). The River Niger water availability: facing future needs and climate change. Global  
1007 Change: Facing Risks and Threats to Water Resources (Proceedings of the Sixth World FRIEND  
1008 Conference, Fez, Morocco, October 2010). IAHS Publications, 340:637-645.
- 1009 Makwana, J. J., & Tiwari, M. K. (2017). Hydrological Stream Flow Modelling using Soil and  
1010 Water Assessment Tool (SWAT) and Neural Networks (NNs) for the Limkheda Watershed,  
1011 Gujarat, India. *Modeling Earth Systemms and Environment*, 3: 635–645.  
1012 <https://doi.org/10.1007/s40808-017-0323-y>
- 1013 Mausbach, M., & Dedrick, A. (2004). The Length We Go Measuring Environmental Benefits of  
1014 Conservation Practices. *Journal of Soil and Water Conservation*, 59(5): 96–103.
- 1015 Microsoft Open Source, McFarland, M., Emanuele, R., Morris, D., & Augspurger, T. (2022).  
1016 microsoft/PlanetaryComputer: October 2022 (2022.10.28). *Zenodo*.  
1017 <https://doi.org/10.5281/zenodo.7261897>
- 1018 Minns, W., & Hall, M. J. (1996). Artificial neural networks as rainfall-runoff models.  
1019 *Hydrological Sciences Journal*, 41, 399–417. <https://doi.org/10.1080/02626669609491511>
- 1020 Mohammadi, B., Moazenzadeh, R., Christian, K., & Duan, Z. (2021). Improving streamflow  
1021 simulation by combining hydrological process-driven and artificial intelligence-based models.

- 1022 *Environmental Science and Pollution Research*, 28, 65752–65768.  
1023 <https://doi.org/10.1007/s11356-021-15563-1>
- 1024 Moran, P. (1970). Simulation and Evaluation of Complex Water Systems Operations, *Water*  
1025 *Resources Research*, 6, 1737–1742. <https://doi.org/10.1029/WR006i006p01737>
- 1026 Muñoz, S. J. (2019). ERA5-Land hourly data from 1950 to present. Copernicus Climate Change  
1027 Service (C3S) Climate Data Store (CDS). <https://doi.org/10.24381/cds.e2161bac> (Accessed on  
1028 12-March-2022).
- 1029 Murphy, K. P. (2022). Probabilistic Machine Learning: An Introduction. *The MIT Press*, ISBN  
1030 9780262046824 pp31-71.
- 1031 Nash, J. E., & Sutcliffe, J. V. (1970). River Flow Forecasting through Conceptual Models Part I  
1032 – A Discussion of Principles. *Journal of Hydrology*, 10, 282–290. [https://doi.org/10.1016/0022-](https://doi.org/10.1016/0022-1694(70)90255-6)  
1033 [1694\(70\)90255-6](https://doi.org/10.1016/0022-1694(70)90255-6)
- 1034 Ni, L., Wang, D., Singh, V. P., Wu, J., Wang, Y., Tao, Y., & Zhang, J. (2020). Streamflow and  
1035 rainfall forecasting by two long short-term memory-based models. *Journal of Hydrology*, 583,  
1036 124296. <https://doi.org/10.1016/j.jhydrol.2019.124296>
- 1037 Noori, N., & Kalin, L. (2016). Coupling SWAT and ANN models for enhanced daily stream  
1038 flow Prediction. *Journal of Hydrology*, 533: 141–151.  
1039 <https://doi.org/10.1016/j.jhydrol.2015.11.050>
- 1040 Oguntunde, P. G., Abiodun, B. J., & Lischeid, G. (2014). A numerical modelling study of the  
1041 hydroclimatology of Niger River Basin, West Africa. *Hydrological Sciences Journal*, 61(1):94-  
1042 106. <https://doi.org/10.1080/02626667.2014.980260>

- 1043 Pfannerstill, M., Björn, G., & Fohrer, N. (2014). Smart Low Flow Signature Metrics for an  
1044 Improved Overall Performance Evaluation of Hydrological Models. *Journal of Hydrology*, 510:  
1045 447–458. <https://doi.org/10.1016/j.jhydrol.2013.12.044>
- 1046 Okpara, J. N., Tarhule, A. A., & Perumal, M. (2013). Study of Climate Change in Niger River  
1047 Basin, West Africa: Reality Not a Myth. *Climate Change – Realities, Impacts Over Ice Cap, Sea*  
1048 *Level and Risks, Edited by Bharat Raj Singh, In Tech*. pp3-37.
- 1049 Persits, F. M., Ahlbrandt, T. S., Tuttle, M. L., Charpentier, R. R., Brownfield, M. E., &  
1050 Takahashi, K. I., (1997). Maps showing geology, oil and gas fields and geological provinces of  
1051 Africa: *U.S. Geological Survey Open-File Report 97-470-A*, <https://doi.org/10.3133/ofr97470A>
- 1052 Poméon, T., Diekkrüger, B., Springer, A., Kusche, J., & Eicker, A. (2018). Multi-Objective  
1053 Validation of SWAT for Sparsely-Gauged West African River Basins—A Remote Sensing  
1054 Approach. *Water*, 10(451). <https://doi.org/10.3390/w10040451>.
- 1055 Pyo, J., Pachepsky, Y., Kim, S., Abbas, A., Kim, M., Kwon, Y. S., et al. (2023). Long short-term  
1056 memory models of water quality in inland water environments. *Water Research X*, 21, 100207.  
1057 <https://doi.org/10.1016/j.wroa.2023.100207>.
- 1058 Pyrcz, M. J., & Deutsch, C. V. (2018). Transforming Data to a Gaussian Distribution. In J. L.  
1059 Deutsch (Ed.), *Geostatistics Lessons*. Retrieved from  
1060 <http://geostatisticslessons.com/lessons/normalscore>
- 1061 Schuol, J., Abbaspour, K. C., Srinivasan, R., & Yang, H. (2008). Estimation of freshwater  
1062 availability in the West African sub-continent using the SWAT hydrologic model. *Journal of*  
1063 *Hydrology*. 352, 30–49. <https://doi.org/10.1016/j.jhydrol.2007.12.025>
- 1064 Singh, D., Vardhan M., Sahu, R., Chatterjee, D., Chauhan, P., & Liu, S. (2023). Machine-  
1065 learning- and deep-learning-based streamflow prediction in a hilly catchment for future scenarios

1066 using CMIP6 GCM data. *Hydrology and Earth System Sciences*, 27, 1047-1075.  
1067 <https://doi.org/10.5194/hess-27-1047-2023>

1068 Sonntag, D. (1990). Important new values of the physical constants of 1986, vapour pressure  
1069 formulations based on the ITS-90, and psychrometer formulae. *Zeitschrift für Meteorologie*,  
1070 40(5), 340–344.

1071 Tibshirani, R. (1996). Regression Shrinkage and Selection Via the Lasso. *Journal of the Royal*  
1072 *Statistical Society: Series B (Methodological)*, 58(1), 267-288. [https://doi.org/10.1111/j.2517-](https://doi.org/10.1111/j.2517-6161.1996.tb02080.x)  
1073 [6161.1996.tb02080.x](https://doi.org/10.1111/j.2517-6161.1996.tb02080.x)

1074 Thompson, J. R., Crawley, A. and Kingston, D. G. (2017). Future river flows and flood extent in  
1075 the Upper Niger and Inner Niger Delta: GCM-related uncertainty using the CMIP5 ensemble.  
1076 *Hydrological Sciences Journal*, 62(14):2239-2265.  
1077 <https://doi.org/10.1080/02626667.2017.1383608>

1078 Van, S. P., Le, H. M., Thanh, D. V., Dang, T. D., Loc, H. H., & Anh, D. T. (2020). Deep  
1079 Learning Convolutional Neural Network in Rainfall–Runoff Modelling. *Journal of*  
1080 *Hydroinformatics*, 22(3), 541–561. <https://doi.org/10.2166/hydro.2020.095>

1081 Viessman Jr. W., & Lewis, G. L. (1996). Introduction to Hydrology, 4th ed. *Harper Collins*,  
1082 New York. p165.

1083 Vizi, Z., Batki, B., Rátki, L., Szalánczi, S., Fehérváry, I., Kozák, P., & Kiss, T. (2023). Water  
1084 level prediction using long short-term memory neural network model for a lowland river: a case  
1085 study on the Tisza River, Central Europe. *Environmental Sciences Europe*, 35(92).  
1086 <https://doi.org/10.1186/s12302-023-00796-3>

- 1087 Vogel, R. M., Lall, U., Cai, X., Rajagopalan, B., Weiskel, P. K., Hooper, R. P., & Matalas, N. C.  
1088 (2015). Hydrology: the interdisciplinary science of water. *Water Resources Research*, 51, 4409–  
1089 4430. <https://doi.org/10.1002/2015WR017049>
- 1090 Xia, J., O'Connor, K. M., Kachroo, R. K., & Liang, G. C. (1997). A non-linear perturbation  
1091 model considering catchment wetness and its application to river flow forecasting. *Journal of*  
1092 *Hydrology*, 200(1-4), 164–178. [https://doi.org/10.1016/S0022-1694\(97\)00013-9](https://doi.org/10.1016/S0022-1694(97)00013-9)
- 1093 Xu, Y., Lin, K., Hu, C., Wang, S., Wu, Q., Zhang, L., & Ran, G. (2023). Deep transfer learning  
1094 based on transformer for flood forecasting in data-sparse basins. *Journal of Hydrology*, 625(A),  
1095 129956. <https://doi.org/10.1016/j.jhydrol.2023.129956>
- 1096 Zanaga, D., Van De Kerchove, R., De Keersmaecker, W., Souverijns, N., Brockmann, C., Quast,  
1097 R., et al. (2021). ESA WorldCover 10 m 2020 v100. <https://doi.org/10.5281/zenodo.5571936>.
- 1098 Zhang, G., Patuwo, B. E., & Hu, M. Y. (1998). Forecasting with artificial neural networks: The  
1099 state of the art. *International Journal of Forecasting*, 14(1), 35–62.  
1100 [https://doi.org/10.1016/S0169-2070\(97\)00044-7](https://doi.org/10.1016/S0169-2070(97)00044-7)